Composites Part B 266 (2023) 110983

Contents lists available at ScienceDirect

Composites Part B

journal homepage: www.elsevier.com/locate/compositesb

Semi-analytical mechanical model for FRCM-to-substrate shear bond tests

Gabriele Milani

Department of Architecture, Built Environment and Construction Engineering, Politecnico di Milano, Piazza Leonardo da Vinci 32, 20133, Milano, Italy

ARTICLE INFO

Handling Editor: Prof. Ole Thomsen

Keywords:
Semi-analytical model
FRCM-to-substrate shear bond tests
Coupled system of differential equations
Debonding of FRCM from substrate
Matrix cracking
Non-linear shear-slip interfaces

ABSTRACT

The debonding process of an FRCM reinforcing system from the substrate is studied in a semi-analytical fashion. FRCM is modeled considering independently the central elastic fiber grid and the two thick upper and lower matrix layers, assumed elasto-fragile; matrix and fiber are considered in a monoaxial state of stress; they mutually exchange shear stresses at the interface, this latter characterized by a softening stress-slip relationship; the reinforcement system is then bonded with a rigid substrate by means of a further elastic interface. Under such hypotheses, a simple system of first order non-linear and coupled differential equations is derived and solved by means of a semi-analytical approach. Independent variables are the axial displacements of the three layers (upper and lower matrix, central fiber) and the corresponding axial stresses. The approach is successfully validated against two experimental datasets available in the literature, relying into different FRCM strengthening systems bonded to rigid substrates and subjected to single lap shear tests. The model is able to capture not only the global debonding behavior but also the local one, with a precise prediction along the bond length of the shape of the axial stresses into the different layers, of the interface shear stresses and of the location of the cracks inside the matrix.

1. Introduction

Existing reinforced concrete and masonry structural elements quite frequently need upgrading, for instance because their load carrying capacity is insufficient in seismic zone or to deal in general with extreme events. In order to cope with such a need, all around the world it is gathering momentum the application of external strengthening systems [1–5], which are characterized by rapid execution, low invasiveness and do not require a partial or total inhibition of use of the structure during the installation. FRCM is an acronym that stands for Fabric Reinforced Cementitious Matrix; also known as TRM (Textile Reinforced Mortar), it relies into a grid of highly resistant dry fiber (carbon, glass, PBO, basalt are four of the most popular materials used) embedded into two layers of mortar typically characterized by very good strength [5]. Instead of fibers, steel cords formed by interwoven steel wires can be used; in this case, more properly, the strengthening system is called Steel Reinforced Grout (SRG).

FRCM is nowadays considered much more suitable than a more traditional strengthening obtained with Fiber Reinforced Polymer (FRP) strips glued with epoxy resins to the substrate, especially in the application on masonry structures; in fact, it is now known that FRPs exhibit a too high stiffness, very low vapor permeability -which over time is responsible for plaster and substrate degradation-, a huge decrease of the performance at high temperature and, most important, it is an intervention considered irreversible, and hence generally not admitted for listed historical buildings.

From a mechanical point of view -an observation confirmed experimentally [6–14]- the increase of the load bearing capacity obtained applying both FRPs and FRCMs substantially occurs for the transfer of tangential stresses from the substrate to the reinforcement; this latter, working in tension, allows to improve considerably the ultimate loads when applied to materials -like masonry- basically unable to withstand tensile stresses.

Consequently, the determination of the debonding properties of a reinforcement is a crucial preliminary step to carry out in a second phase sufficiently predictive simulations on real scale structural elements, where the role played by FRCM in increasing strength and ductility is taken into account in a realistic manner. Undoubtably, the main application of such externally mounted composite systems may involve also bending [15] and out-of-plane deformations, especially near the damaged regions, where the stress state at the reinforcement-support interface is characterized by considerable complexity, mainly because normal internal actions are coupled with shear, as also confirmed by the recent experimental literature available [16–18]. To achieve such goal, it is first necessary to have an insight into the expected behavior under standardized prescribed conditions, where mode II and mode I failures

E-mail address: gabriele.milani@polimi.it.

https://doi.org/10.1016/j.compositesb.2023.110983
Received 23 April 2023; Received in revised form 25 August 2023; Accepted 3 September 2023
Available online 4 September 2023

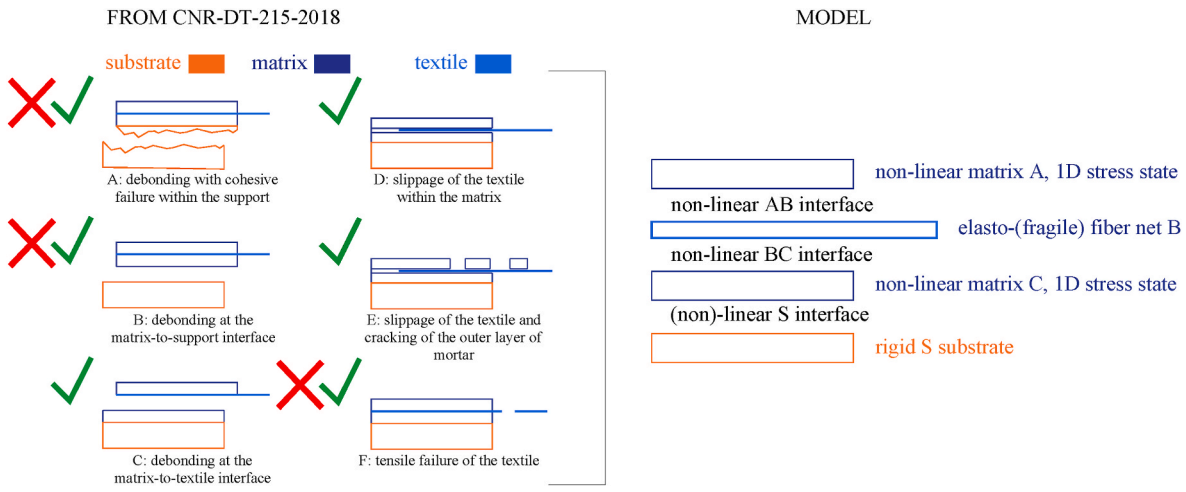

Fig. 1. Modes of failure observed experimentally in a standard debonding test (left) and mechanical properties to assume for the different components of the reinforcement to properly simulate them (right).

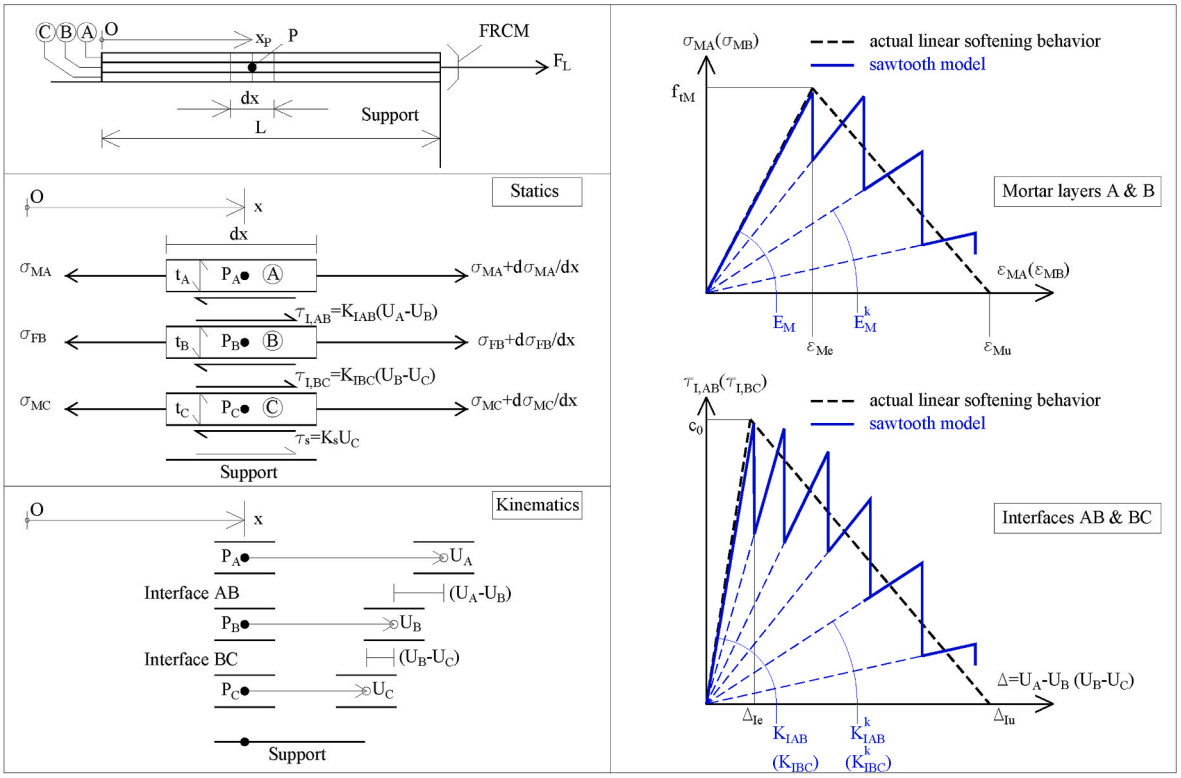

Fig. 2. Mechanical model adopted to study numerically the bond behavior of an FRCM applied to an infinitely stiff substrate.

are decoupled. According to many experimental works nowadays available, the single lap shear test carried out on flat reinforced specimens is one of the crucial tests -along with the coupon and the peeling test- to characterize with a certain level of reliability the expected behavior under more complex loading and geometric conditions. Focusing on the debonding test, the experimental characterization of the interface between substrate and FRCM is not as easy as for FRPs and innovative techniques are needed, as those proposed for instance in Ref. [19,20], but still some major problems are far to be overcome.

Remaining to deal with mechanical matters and leaving apart experimental issues, it appears crucial to figure out how much the transfer of internal actions is effective. For FRPs, there is a well-documented literature showing that a key role is played by the interface between reinforcement and substrate. The interpretation of the mechanical behavior is simpler and the standard approach to investigate quantitatively the efficacy of the reinforcement is without any doubt the delamination test, where a strip with a certain length is glued to the support and then axially loaded at one edge with the counter-lateral left free, up to the complete detachment.

By its very nature, an FRCM reinforcement is more complex, because constituted by many different elements that can behave non-linearly, typically the two inorganic matrix layers and more than one interface, the most important being those between fiber and matrix.

It is not a case, indeed, that the observed modes of failure are various, depending on the mechanical properties of the different materials constituting the reinforcement. According to the Italian Guidelines CNR-

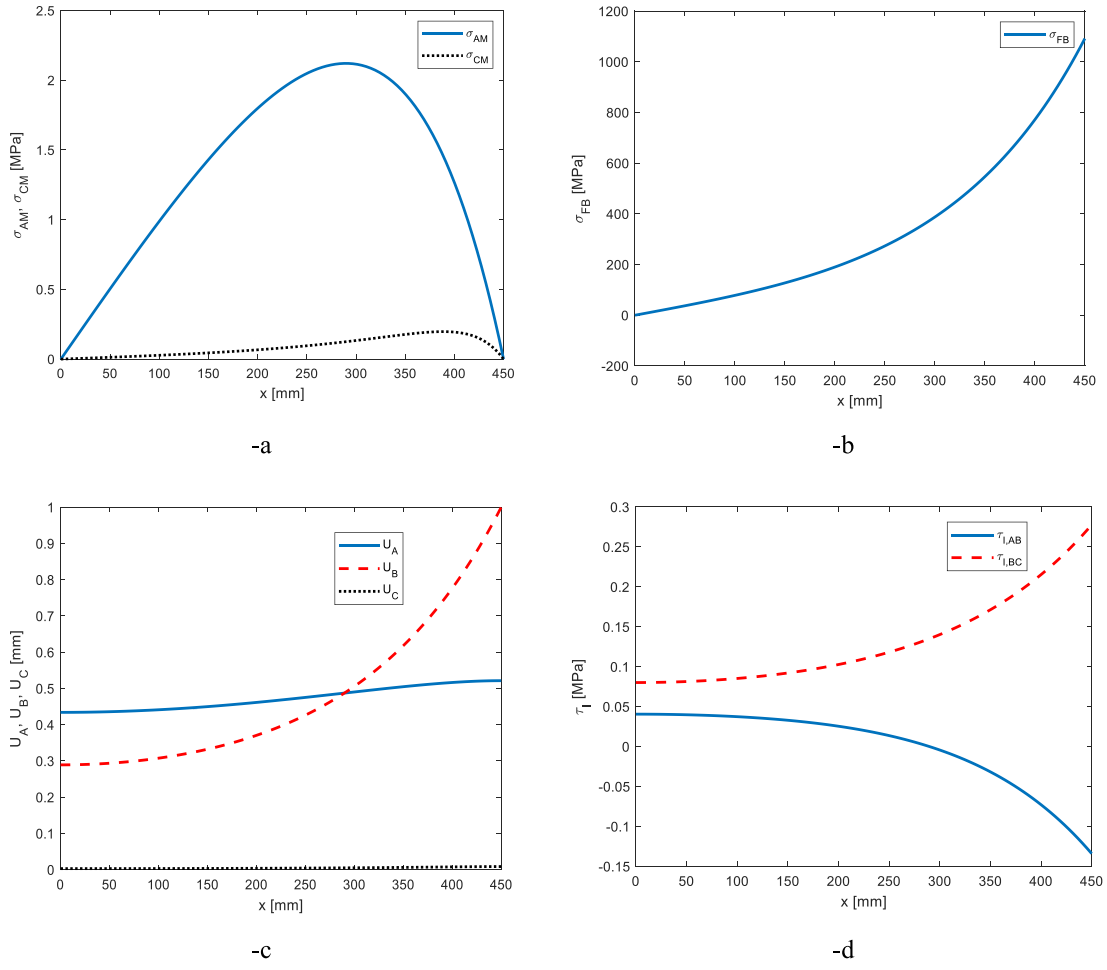

Fig. 3. Elastic solutions for a case of technical relevance (L = 450 mm, $t_A = t_C = 4$ mm, $t_B = 0.054$ mm, $K_{IAB} = K_{IBC} = 0.28\ \frac{N}{mm^3}$, $K_s = 100K_{IAB}$, $E_M = 7000\ \frac{N}{mm^2}$, $E_F = 206000\ \frac{N}{mm^2}$ and $U_{BL} = 1$ mm). -a: σ_{MA} and σ_{MC} stresses along the bonded length x. -b: stress in the fiber σ_{FB}. -c: U_A, U_B and U_C. -d: tangential stresses $\tau_{I,AB}$ and $\tau_{I,BC}$ acting on AB and BC interfaces.

DT-2015 (2018), see Fig. 1, they are 6, namely the debonding with a cohesive failure inside the support (A), the debonding at the interface between support and inner matrix layer (B), the debonding at the interface between fiber textile and inner matrix (C), the slippage of the textile inside the mortar layers respectively without (D) and with external matrix cracking (E) and the tensile failure of the interface (F).

In order to predict the global behavior, from a numerical point of view, following what already presented in the literature for FRPs [21–35], a relatively straightforward strategy is to lump the non-linearity at the reinforcement-support interface (i.e. adapting the approach used for FRPs [36–43]). The latter- is a quite standard and generalist strategy which proved to be predictive in terms of results, at least looking at the global force-displacement curves obtained experimentally. In particular, there are models that, assuming multi-linear or exponential-softening constitutive laws for the interface, allow to derive closed form mathematical expressions for the internal variables (static and kinematic); in alternative, some other approaches are at disposal, where the field equations have been solved numerically as classic Boundary Value Problem BVP or transformed into problems with initial conditions imposed (Cauchy's Problem), which are characterized by the great advantage of being fully explicit. However, an insight into the actual distribution of stresses inside the different layers constituting the reinforcement system turns out to be almost totally lost, and the local redistribution of stresses during the loading process -for instance when one of the matrix layers cracks-cannot be either predicted or reproduced as it occurs in reality during an experimental test.

In few recent literature, see e.g. Refs. [44–48], relatively novel models that take into account separately the elastic reinforcing grid, the brittle mortar layers and the interface between them have been proposed; typically, for FRCM, a non-linear system of differential equations governs the problem, which is hard to be solved by means of conventional numerical methods and typically requires some simplifications to boost stability of the algorithms. For instance, in Ref. [46], the external matrix layer is not considered and a specifically crafted method based on a shooting technique to transform the BVP into one at initial conditions imposed has been proposed. In any case, all the previous models appear more advanced than those based on lumping the non-linearity exclusively at the interface, because able to give locally much more information on the debonding phenomenon. A straightforward alternative -which has been originally used for FRPs [49–52]- is to discretize each component of the reinforcement system into FEs, see e.g. Refs. [53–56], then adopting for matrix and interfaces the non-linear material models already available in the specific commercial code used; such way of proceeding is however characterized by many drawbacks: for instance, to predict the behavior of a different specimen subjected to single or double lap shear tests would require a completely new calibration in terms of discretization and material properties to assign and the user would be forced to adapt such calibration considering what is actually available in the software, which obviously is not conceived to deal only with such a specific, highly complex mechanical problem. Anyway,

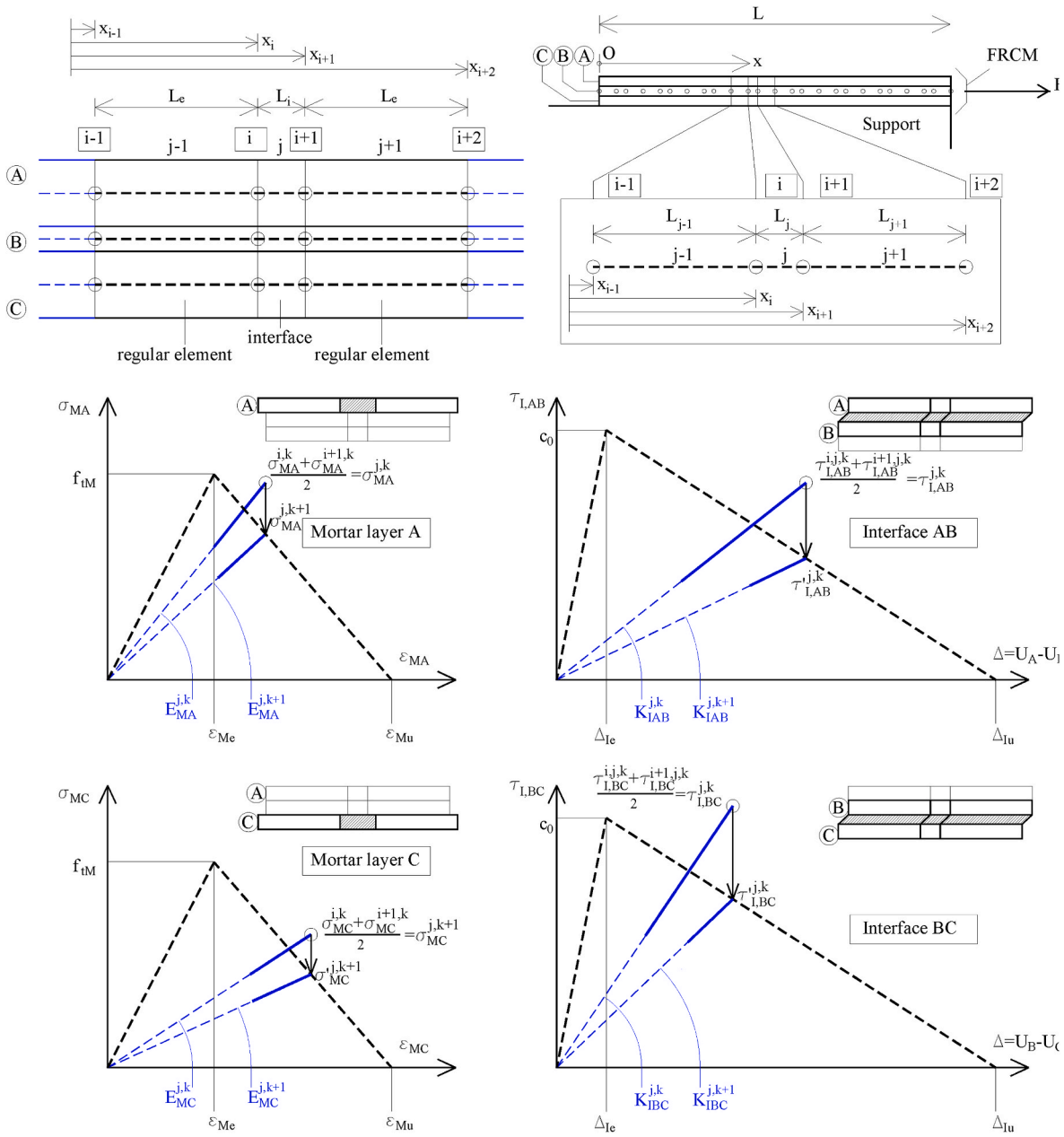

Fig. 4. Reformulation of the problem with non-linear materials. Subdivision into elements with lumped non-linearity on mortar layers and updating strategy of the elastic properties at time step k + 1.

what is clear from a thorough review of the existing literature is that there is still a need for a sound interpretation of the experimental data observed, at least as far as the local behavior is concerned.

The model proposed here is a semi-analytical one: an FRCM strengthening system is assumed characterized by three different layers (upper and lower matrix with central fiber grid embedded), exchanging at the interface shear stresses. Mortar matrix is assumed elasto-fragile and the fiber grid linear elastic. The interfaces between the layers are assumed characterized by an elasto-fragile shear stress-slip relationship. The reinforcing system is finally bonded to the substrate by means of an elastic interface. Consistently with such modeling strategy, modes of failure labeled in Fig. 1 as C, D and E are correctly reproduced. At least in principle, modes B and F can be also simulated, if it is imposed respectively a non-linear behavior of the interface between support and inner matrix layer and an elastic-perfectly fragile constitutive law for textile. Mode A is more difficult to take into consideration, but suitably modifying the tau-slip relation of the support-to-matrix interface, there is the possibility to reproduce -albeit in an approximate way-the damage spreading in the bulk. No matter about the particular stress-strain relationships assumed for the different components of the FRCM reinforcement, independent variables are the axial displacements of the three layers (upper and lower matrix, central fiber) and the corresponding axial stresses. Under such assumptions, a simple system of first order non-linear and coupled differential equations is derived and solved by means of a semi-analytical approach. The mathematical model is successfully validated against two experimental datasets available in the literature, consisting of different FRCM strengthening systems bonded to bricks and masonry substrates and subjected to single lap shear tests. The model is able to capture not only the global debonding behavior but also the local one, with a precise prediction along the bond length of the shape of the axial stresses into the different layers, of the interface shear stresses and of the location of the cracks inside the matrix.

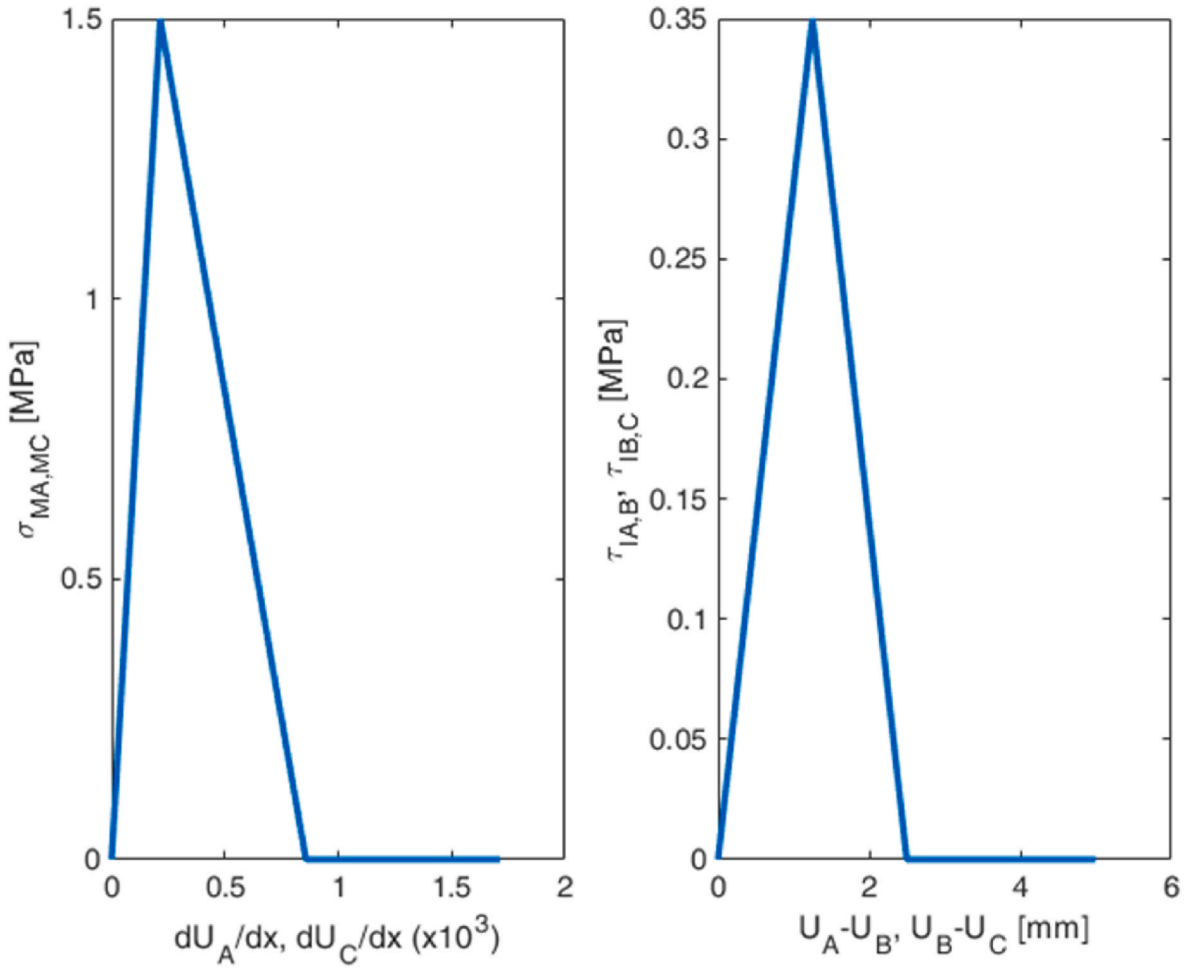

Fig. 5. Benchmark 0. Mechanical properties assumed for the mortar layers A & C and for the interface between mortar and fiber.

Table 1
Benchmark 0. Geometric properties of the reinforcement system.

Symbol	Description		UoM
$t_A = t_C$	Layer A & C thickness	4	mm
t_B	Layer B thickness	0.054	mm
E_B	Fiber elastic modulus	206000	MPa
L	Bond length	450	mm

2. The mathematical model in brief

The model proposed is aimed at reproducing FRCM debonding in a single lap shear test, Fig. 2. FRCM is assumed constituted by three layers, denoted as A (external mortar), B (fiber net) and C (internal mortar). Layer C is glued to the support. The model is mono-dimensional and kinematic variables are the axial displacements of the layers, named from the extrados to the intrados with U_A, U_B and U_C respectively. L is the bonded length and the thickness of the layers is t_A, t_B and t_C. The out-of-plane width is assumed unitary. Between layers A and B a tangential stress $\tau_{I,AB}$ is exchanged at the interface; similarly, $\tau_{I,BC}$ is exchanged between layers B and C.

2.1. Solution with linear elastic materials

Mortar is assumed to behave in tension in a linearly brittle way, the fiber is elastic whereas a linear softening law is adopted for the interfaces between mortar and fiber, see Fig. 2. The support is assumed linear elastic and its effect on the global deformability of the reinforcing pack is taken into account with the stiffness constant K_s. The model is multilinear, i.e. mortar and interfaces non-linear behavior is approximated with sawtooth functions. First, it is therefore crucial to formulate the mechanical properties assuming all materials linear elastic. In this regard, let denote the elastic modulus of mortar with E_M, that of the fiber with E_F and with K_{IAB} (K_{IBC}) the elastic stiffness of the interface between A and B (B and C), respectively.

Within the mono-axial behavior assumption for fiber and mortar layers, provided that interfaces, mortar and support are linear elastic, it is possible to write the following equilibrium and constitutive relationships:

$$\begin{aligned}
\sigma_{MA} &= E_M \frac{dU_A}{dx} \\
\sigma_{FB} &= E_F \frac{dU_B}{dx} \\
\sigma_{MC} &= E_M \frac{dU_C}{dx} \\
\frac{d\sigma_{MA}}{dx} &= \frac{K_{IAB}(U_A - U_B)}{t_A} \\
\frac{d\sigma_{FB}}{dx} &= \frac{K_{IBC}(U_B - U_C) - K_{IAB}(U_A - U_B)}{t_B} \\
\frac{d\sigma_{MC}}{dx} &= -\frac{K_{IBC}(U_B - U_C)}{t_C} + \frac{K_s U_C}{t_C}
\end{aligned} \tag{1}$$

Where σ_{MA}, σ_{FB} and σ_{MC} are the tensile stresses acting on layer A, B and C respectively and all the other symbols have been already introduced. Eq.

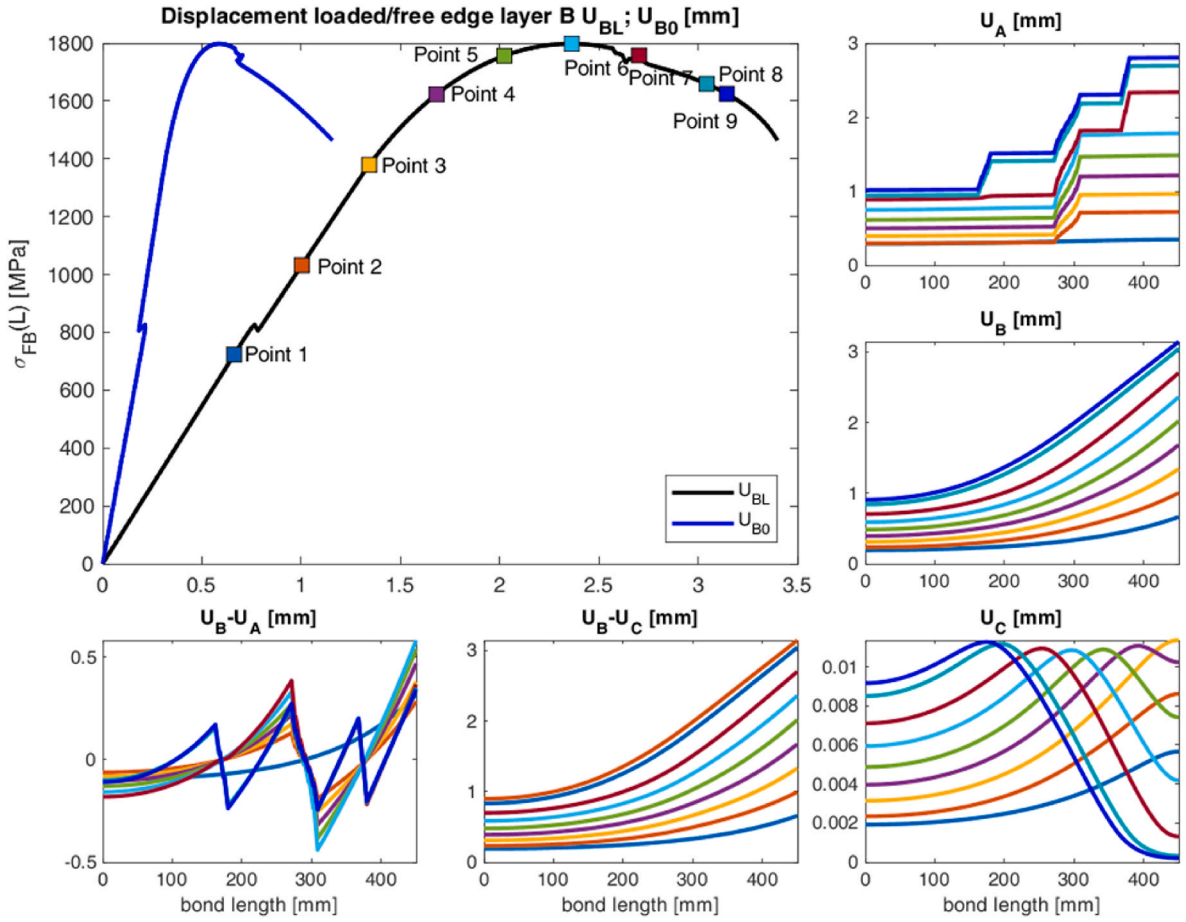

Fig. 6. Benchmark 0. From the top-left in clockwise order. Stress $\sigma_{FB}(L)$ - displacements U_{BL}, U_{B0} curves; $U_A, U_B, U_C, U_B - U_C, U_B - U_A$ behavior along the bond length (the color of the curves corresponds to the particular instants investigated during the loading process and match those of the points represented in the top-left sub-figure). (For interpretation of the references to color in this figure legend, the reader is referred to the Web version of this article.)

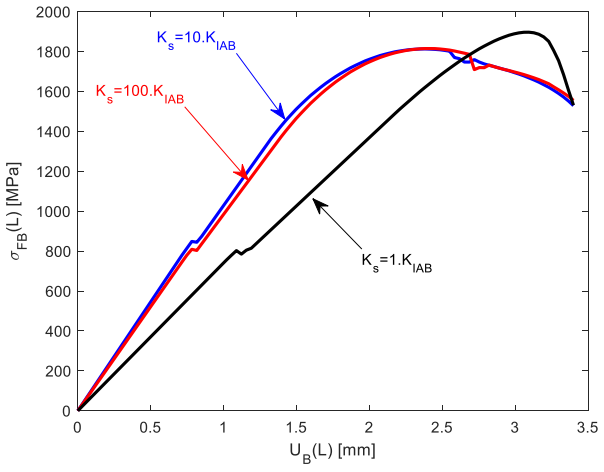

Fig. 7. Sensitivity analysis varying the stiffness of the support-to-inner-matrix interface.

(1) can be rearranged in the following matrix form:

$$\frac{d\mathbf{Y}}{dx} = \begin{bmatrix} \frac{dU_A}{dx} \\ \frac{dU_B}{dx} \\ \frac{dU_C}{dx} \\ \frac{d\sigma_{MA}}{dx} \\ \frac{d\sigma_{FB}}{dx} \\ \frac{d\sigma_{MC}}{dx} \end{bmatrix} = \begin{bmatrix} 0 & 0 & 0 & \frac{1}{E_M} & 0 & 0 \\ 0 & 0 & 0 & 0 & \frac{1}{E_F} & 0 \\ 0 & 0 & 0 & 0 & 0 & \frac{1}{E_M} \\ \frac{K_{IAB}}{t_A} & -\frac{K_{IAB}}{t_A} & 0 & 0 & 0 & 0 \\ -\frac{K_{IAB}}{t_B} & \frac{K_{IBC}+K_{IAB}}{t_B} & -\frac{K_{IBC}}{t_B} & 0 & 0 & 0 \\ 0 & -\frac{K_{IBC}}{t_C} & \frac{K_{IBC}+K_s}{t_C} & 0 & 0 & 0 \end{bmatrix} \begin{bmatrix} U_A \\ U_B \\ U_C \\ \sigma_{MA} \\ \sigma_{FB} \\ \sigma_{MC} \end{bmatrix} = \mathbf{KY} \tag{2}$$

Eq. (2) is a first order ODE system whose solution can be found analytically evaluating the eigenvectors and eigenvalues of $\mathbf{K}$. Let indicate with $\mathbf{E}_V$ and $\text{diag}(\mathbf{E}) = \{\lambda_1\ \lambda_2\ \lambda_3\ \lambda_4\ \lambda_5\ \lambda_6\}$ the eigenvector and eigenvalue matrix, respectively. For the problem at hand, it is interesting to notice that eigenvalues are real and that the solution vector is the following:

$$\mathbf{Y} = C_1\mathbf{E}_{V1}e^{\lambda_1 x} + C_2\mathbf{E}_{V2}e^{\lambda_2 x} + C_3\mathbf{E}_{V3}e^{\lambda_3 x} + C_4\mathbf{E}_{V4}e^{\lambda_4 x} + C_5\mathbf{E}_{V5}e^{\lambda_5 x} + C_6\mathbf{E}_{V6}e^{\lambda_6 x} \tag{3}$$

Where $\mathbf{E}_{Vi}$ is the i-th column of the eigenvectors matrix and C_i are integration constants that can be determined imposing suitable bound-

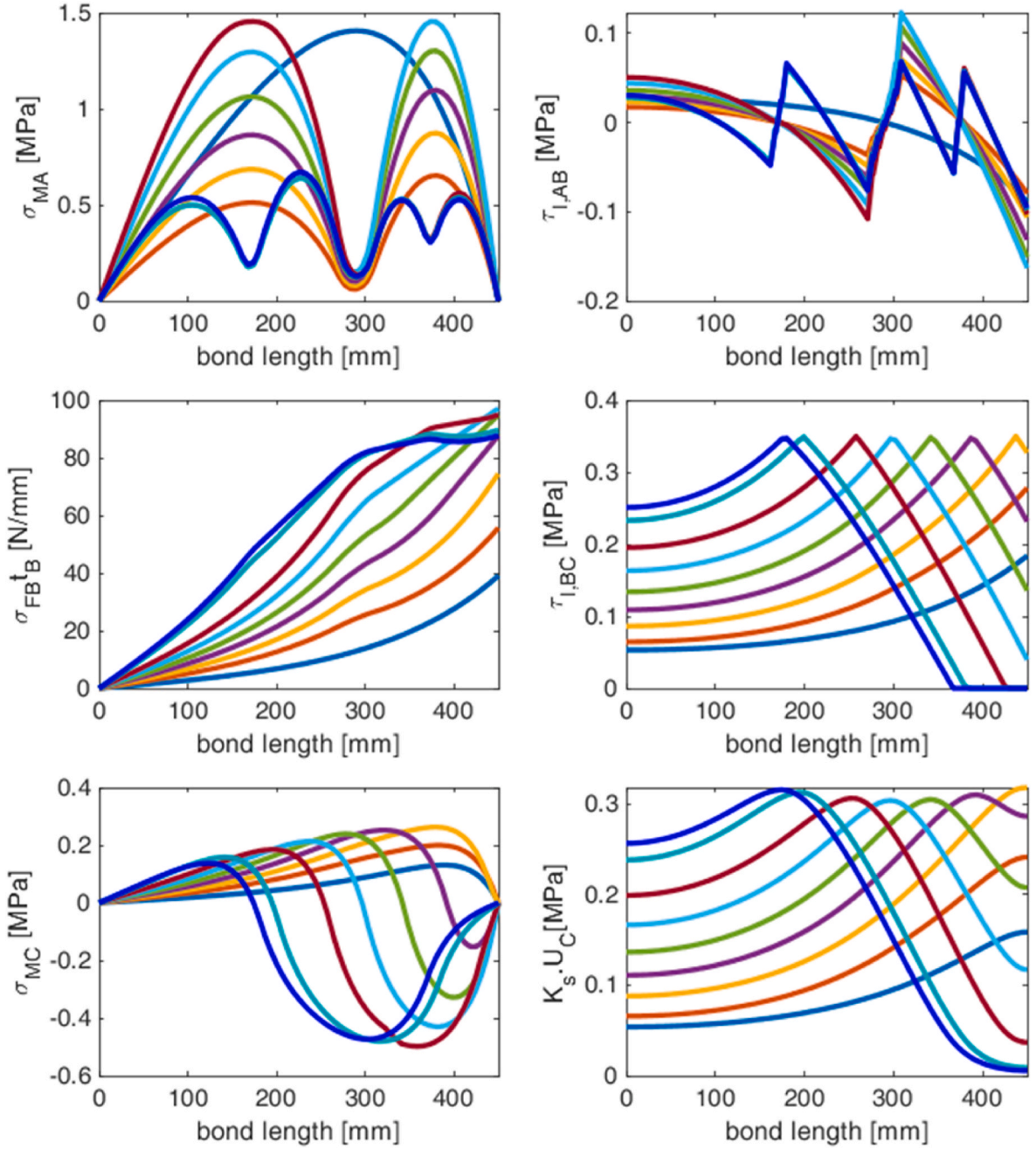

Fig. 8. Benchmark 0. From the top-left in clockwise order. $\sigma_{MA}, \tau_{I,AB}, \tau_{I,BC}, K_s U_C, \sigma_{MC}, \sigma_{FB} t_B$ behavior along the bond length (the color of the curves corresponds to the particular instants investigated during the loading process and match those of the points represented in the previous sub-figure). (For interpretation of the references to color in this figure legend, the reader is referred to the Web version of this article.)

ary conditions. In such kind of Boundary Value Problem BVP, they are the following:

$$\begin{aligned} &\sigma_{MA}(0) = 0 \\ &\sigma_{MC}(0) = 0 \\ &\sigma_{MC}(0) = 0 \\ &\sigma_{MA}(L) = 0 \\ &\sigma_{MC}(L) = 0 \\ &U_B(L) = U_{BL} \end{aligned} \tag{4}$$

Where U_{BL} is the displacement applied at the loaded edge (a displacement control experimental test is considered).

In Fig. 3 it is represented a solution of the elastic problem (taken from the literature [41,46] and discussed further in the following sections in the non-linear range) assuming the following geometric and mechanical properties: $L = 450$ mm, $t_A = t_C = 4$ mm, $t_B = 0.054$ mm, $K_{IAB} = K_{IBC} = 0.28 \frac{N}{mm^3}$, $K_s = 100 K_{IAB}$, $E_M = 7000 \frac{N}{mm^2}$, $E_F = 206000 \frac{N}{mm^2}$ and $U_{BL} = 1$ mm. In particular, subfigure -a depicts σ_{MA} and σ_{MC} stresses along the bonded length x, subfigure -b the normal stress in the fiber (layer B, σ_{FB}), subfigure -c the displacements U_A, U_B and U_C, subfigure -d the tangential stresses $\tau_{I,AB}$ and $\tau_{I,BC}$.

It is finally interesting to point out one of the major limitations of the mechanical model adopted -clearly evident from the results depicted in Fig. 3-d and typical of any kind of schematization by means of interfaces-, namely the inability to impose extra-boundary conditions of zero shear at the free edges ($x = 0$, $x = L$) for the interface AB and BC. In fact, by reductio ad absurdum, imposing a zero shear at the free edges would result into the introduction of the following 4 additional equality constraints:

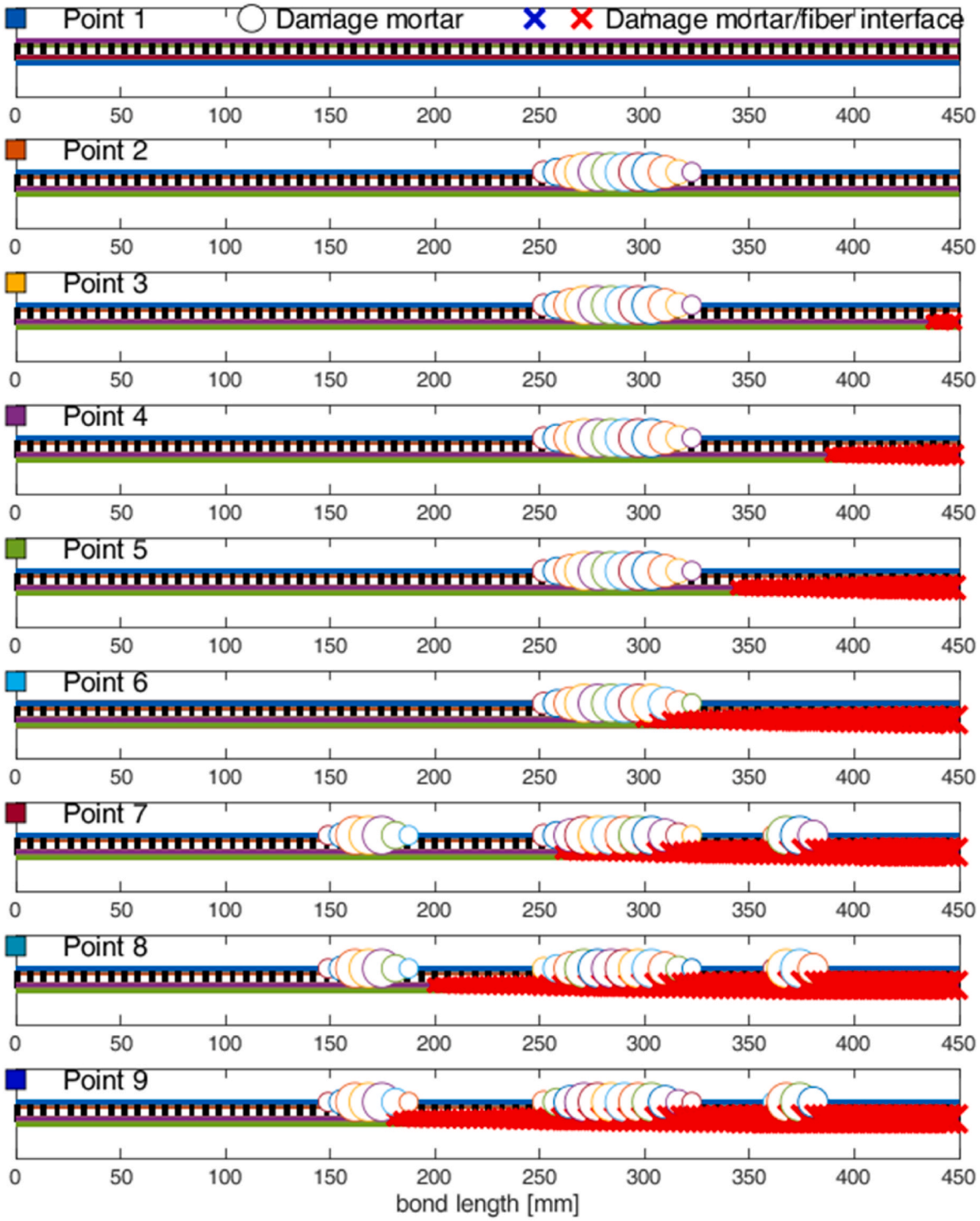

Fig. 9. Benchmark 0. Propagation of damage inside mortar layers and interfaces at the different instants investigated during the loading process. White circles and blue/red crosses represent mortar and interface damage, respectively. Their dimension is proportional to the amount of damage. (For interpretation of the references to color in this figure legend, the reader is referred to the Web version of this article.)

$$\begin{aligned} U_A(0) &= U_B(0) \\ U_B(0) &= U_C(0) \\ U_A(L) &= U_B(L) \\ U_B(L) &= U_C(L) \end{aligned} \tag{5}$$

The linear system to solve would be therefore characterized -at least mathematically-by an over-constraintment, being 6 the unknowns and 10 the linear equations to impose according to the BCs. The system would be therefore impossible.

2.2. Non-linear materials

In the present Section, the numerical procedure adopted to deal with the non-linear behavior of mortar and mortar-fiber interfaces is discussed.

When the materials are assumed non-linear, a discretization with n_e elements of length L_e and $n_e - 1$ small elements of length L_i where all mortar nonlinearity is lumped is assumed. A generic discretization is shown in Fig. 4. Layers A and C remain linear for all the elements with

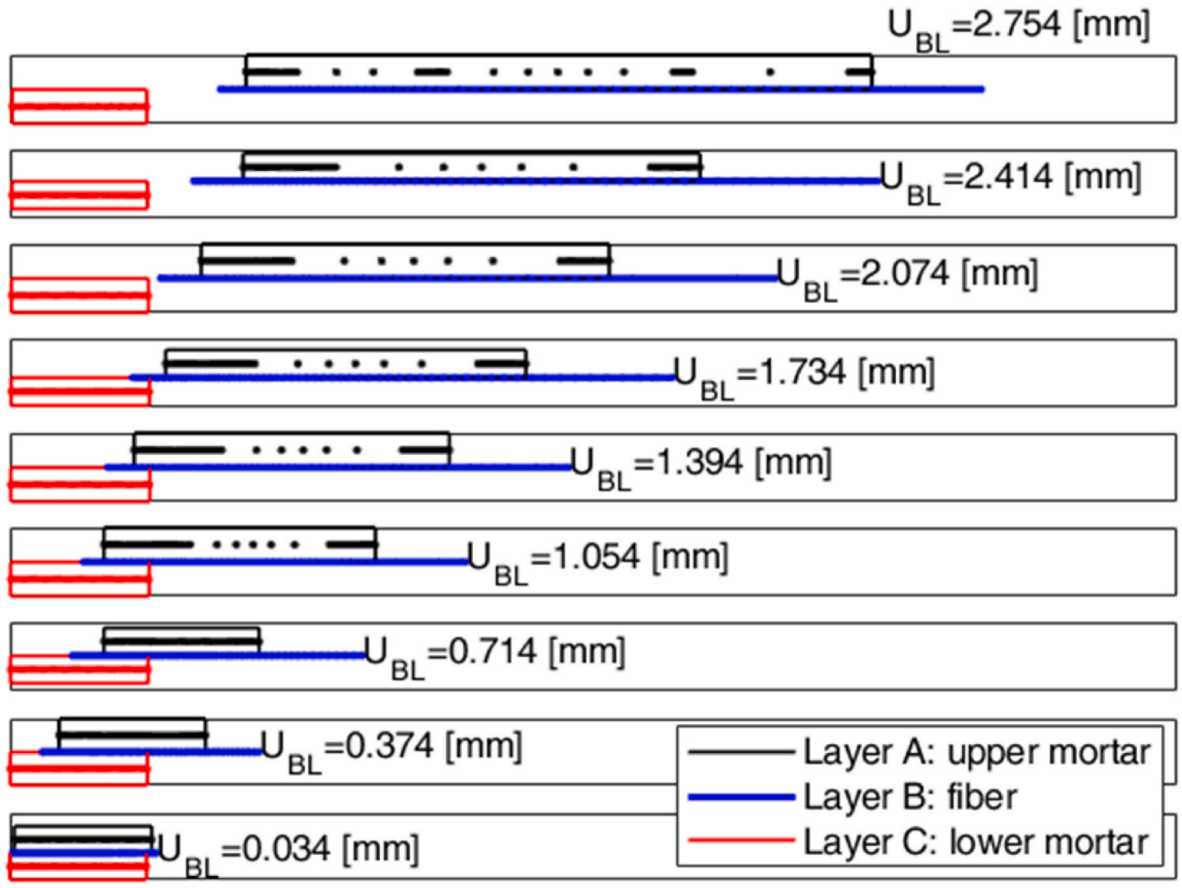

Fig. 10. Benchmark 0. Deformed shapes of the reinforcement system. Snapshots taken at nine values of the displacement U_{BL} applied at the loaded edge.

length L_e. Layer B is always assumed elastic. The strategy adopted to model mortar non-linearity aims at avoiding any issue related to deformation concentration and mesh dependence in softening materials. To concentrate mortar non-linearity exclusively on small interfaces with finite (small) thickness reduces the problem to a discrete mechanical system constituted by elastic elements connected by non-linear interfaces. The interfaces between mortar and fiber, on the contrary, are assumed non-linear everywhere.

The introduction of the periodically distributed damaging elements aims at representing numerically cracking of the brittle mortar under tension in a straightforward and simple manner.

However, from a physical point of view, it should be noted that typically cracks in mortar layer are associated with a material separation between the left and right part in correspondence of the crack. Consequently, in all those positions where cracks are open, the concept of introducing an interface between mortar layer and fiber textile loses physical meaning. This implies that the stiffness of the relevant interface should drop to zero in those regions as well. Such coupling is not reproducible with the model proposed, albeit it could provide a better representation of the physical phenomenon.

Returning back to the general treatment of the non-linearity, it is tackled by means of a sequence of linear problems, in agreement with the strategy proposed in a family of recent papers [57–61] dealing with quasi brittle materials and structures in general, where the stiffness of the elements is progressively reduced in the softening branch, see Fig. 4.

Consistently with such strategy, mortar uniaxial stress-strain and fiber/mortar interface shear stress-slip constitutive relationships are assumed non-linear and approximated with saw tooth laws, as depicted in Fig. 2. The sawtooth laws are not assigned at the beginning of the computations, but the elastic modulus (or stiffness) is progressively reduced at each load step k, according to a specific algorithm that is detailed in what follows. Any nonlinear stress-strain (or shear stress-slip) behavior can be approximated, but here for the sake of simplicity a linear softening is adopted. For mortar, in compression, it is reasonable to assume an infinitely linear response, since the material used for FRCM reinforcement is usually characterized by a quite good compressive strength.

Under such assumptions, each element j of length L_j is elastic at a certain load step k and an analytical solution can be found according to the approach discussed in the previous section. Six integration constants per element should be determined, say $C_q^{j,k}$, according to the imposition of suitable boundary conditions that are discussed hereafter.

Let us indicate with $E_{Me}^{j,k}$, $E_{Mi}^{j,k}$, $K_{IAB}^{j,k}$ and $K_{IBC}^{j,k}$ respectively the extrados mortar layer elastic modulus, the intrados mortar layer elastic modulus, the stiffness of the AB interface and the stiffness of the BC interface at the load step k. The matrix $\mathbf{K}^{j,k}$ of the coefficients in Eq. (2) is therefore the following:

$$\mathbf{K}^{j,k} = \begin{bmatrix} 0 & 0 & 0 & \frac{1}{E_{Me}^{j,k}} & 0 & 0 \\ 0 & 0 & 0 & 0 & \frac{1}{E_F} & 0 \\ 0 & 0 & 0 & 0 & 0 & \frac{1}{E_{Mi}^{j,k}} \\ \frac{K_{IAB}^{j,k}}{t_A} & -\frac{K_{IAB}^{j,k}}{t_A} & 0 & 0 & 0 & 0 \\ -\frac{K_{IAB}^{j,k}}{t_B} & \frac{K_{IBC}^{j,k}+K_{IAB}^{j,k}}{t_B} & -\frac{K_{IBC}^{j,k}}{t_B} & 0 & 0 & 0 \\ 0 & -\frac{K_{IBC}^{j,k}}{t_C} & \frac{K_{IBC}^{j,k}+K_s}{t_C} & 0 & 0 & 0 \end{bmatrix} \tag{6}$$

The solution of the system of first order differential equations

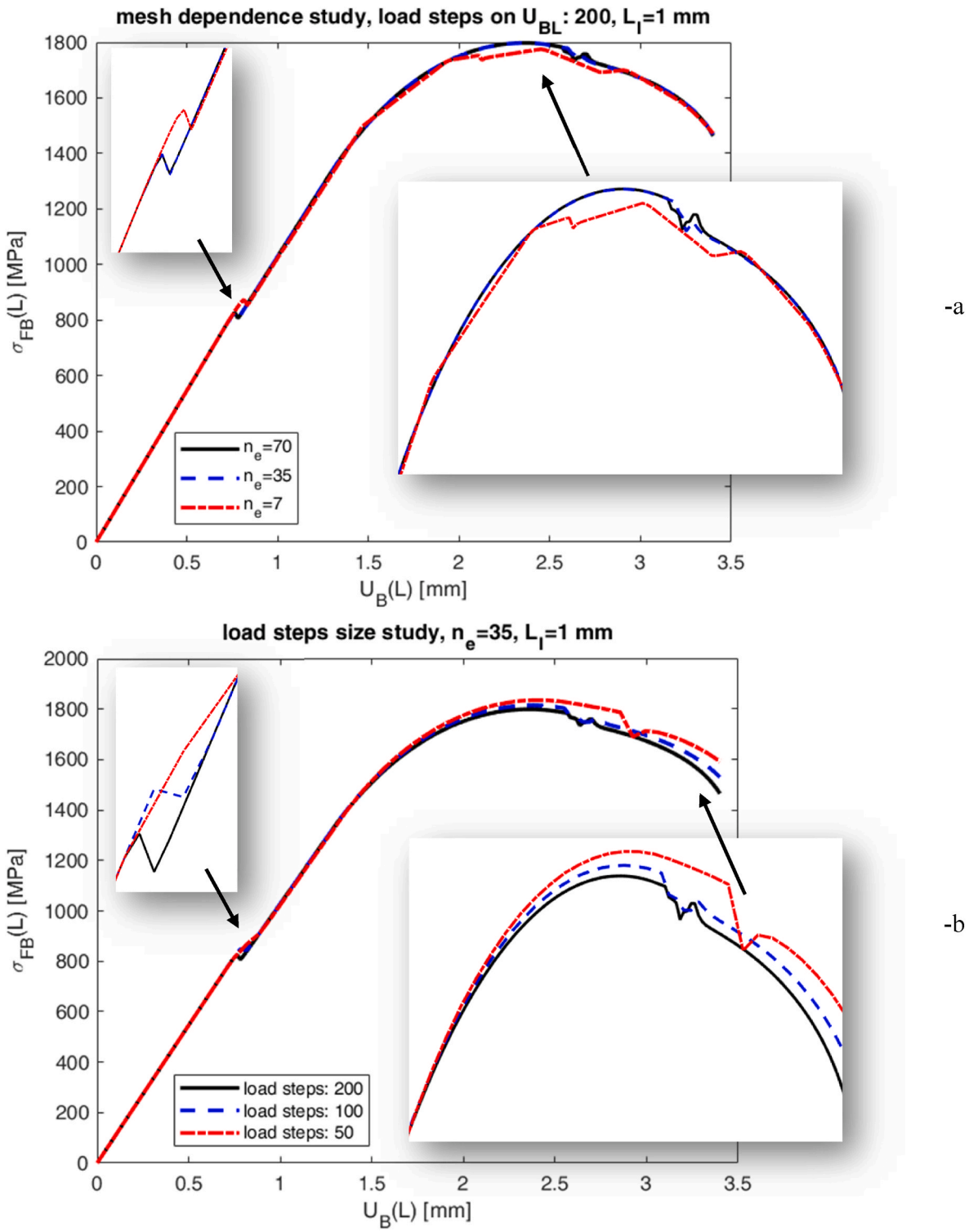

Fig. 11. Benchmark 0. Sensitivity of the results obtained (global response) changing mesh size (-a) and load steps used (-b).

Table 2
Ascione et al. (2015) experimental data. Reinforcement and matrix properties.

Label	reinforcement				matrix			
	type	E_F [MPa]	t_B [mm]	L [mm]	type	E_M [MPa]	f_{tM} [MPa]	$t_A = t_C$ [mm]
Ascione et al. (2015)	steel	183900	0.084	200	mineral-natural hydraulic lime	11400	5.4	5

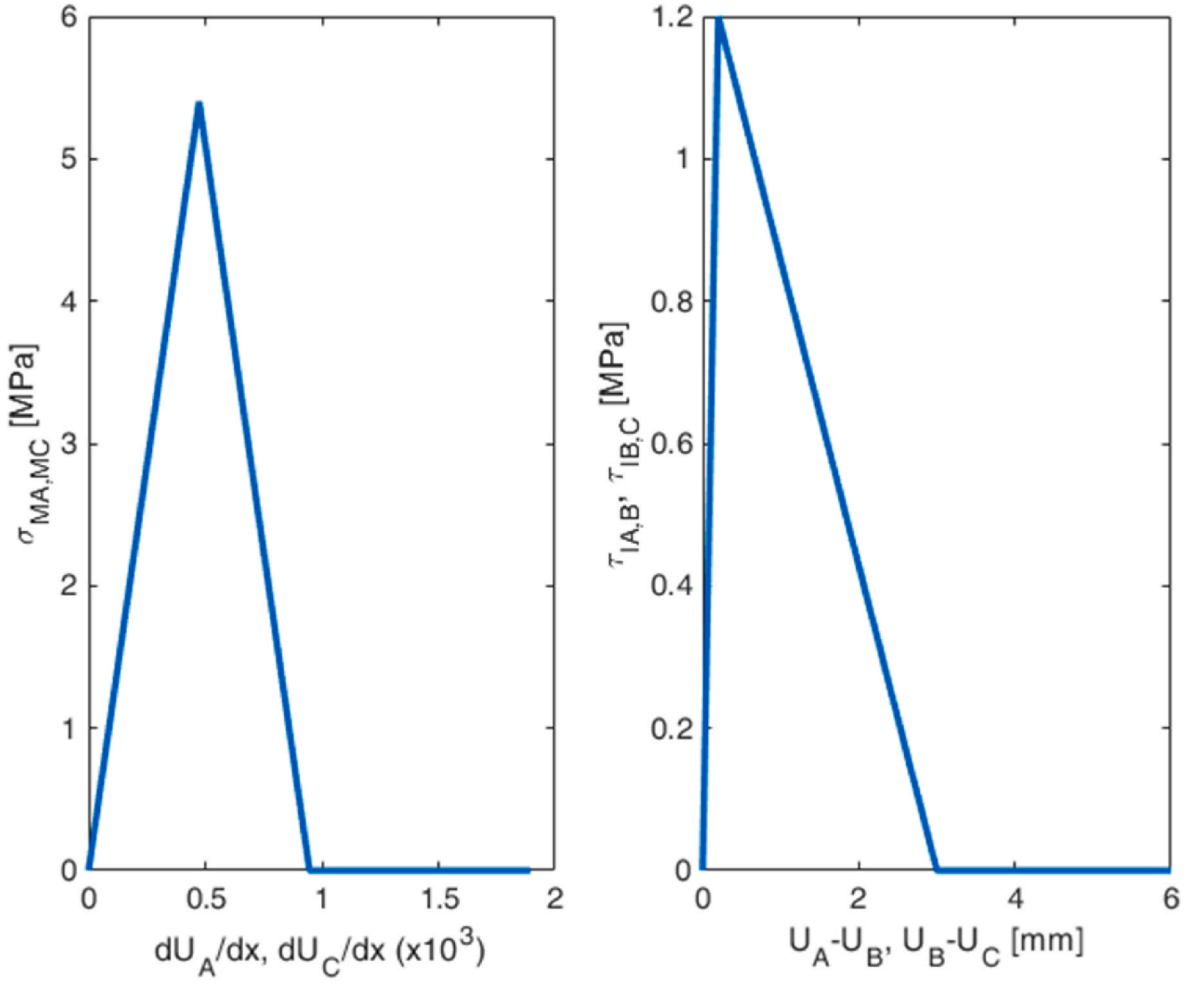

Fig. 12. Ascione et al. (2015) data. Monoaxial stress-strain behavior assumed for mortar layers A & C (left) and shear stress-slip relationship of the interfaces between layers AB & BC (right).

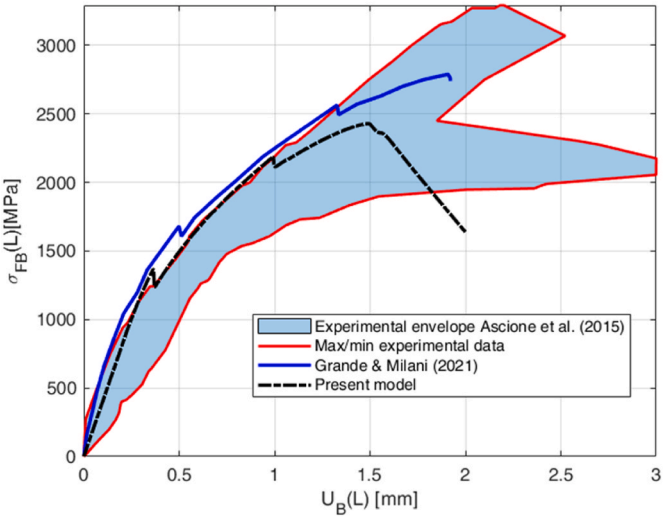

Fig. 13. Ascione et al. (2015) data. Global behavior. Comparison among present model, numerical curve obtained by Grande & Milani [45] and experimental data envelope.

representing the field problem for a single element j is formally identical to the fully elastic case, i.e.:

$$\mathbf{Y}^{j,k}\left(\mathbf{C}_q^{j,k},x\right)=\mathbf{C}_1^{j,k}\mathbf{E}_{V1}^{j,k}e^{\lambda_1^{j,k}x}+\mathbf{C}_2^{j,k}\mathbf{E}_{V2}^{j,k}e^{\lambda_2^{j,k}x}+\mathbf{C}_3^{j,k}\mathbf{E}_{V3}^{j,k}e^{\lambda_3^{j,k}x}+\mathbf{C}_4^{j,k}\mathbf{E}_{V4}^{j,k}e^{\lambda_4^{j,k}x}+\mathbf{C}_5^{j,k}\mathbf{E}_{V5}^{j,k}e^{\lambda_5^{j,k}x}+\mathbf{C}_6^{j,k}\mathbf{E}_{V6}^{j,k}e^{\lambda_6^{j,k}x} \tag{7}$$

Where, apart the symbols already introduced, $\mathbf{Y}^{j,k}$, $\mathbf{E}_{Vq}^{j,k}$ and $\lambda_q^{j,k}$ with $q=1,\ldots,6$ are respectively the solution vector, the eigenvectors and the eigenvalues pertaining to element j at the load step k.

For all elements except the first one located at the free edge, the continuity of the stresses and displacements between elements $j-1/j$ should be imposed. Therefore, the following 6 equations are written in the 12 unknowns $\mathbf{C}_q^{j,k}$ and $\mathbf{C}_q^{j-1,k}$:

$$-\mathbf{Y}^{j-1,k}\left(\mathbf{C}_q^{j-1,k},x_i\right)+\mathbf{Y}^{j,k}\left(\mathbf{C}_q^{j,k},x_i\right)=\mathbf{0}_{6\times1} \tag{8}$$

Where $\mathbf{0}_{6\times1}$ is a 6×1 vector of all zeros and the position of the node i is univocally identified by the abscissa x_i, see Fig. 4.

Eq. (8) should be written for all nodes, excluding the first node located at the free edge and the last one at the loaded edge, therefore $12n_e-12$ equalities are derived.

For the free edge node, the following 3 equations are written, imposing that the normal stress on the three layers A-C is equal to zero:

$$\mathrm{diag}(0\quad 0\quad 0\quad 1\quad 1\quad 1)\mathbf{Y}^{1,k}\left(\mathbf{C}_q^{1,k},0\right)=\mathbf{0}_{6\times1} \tag{9}$$

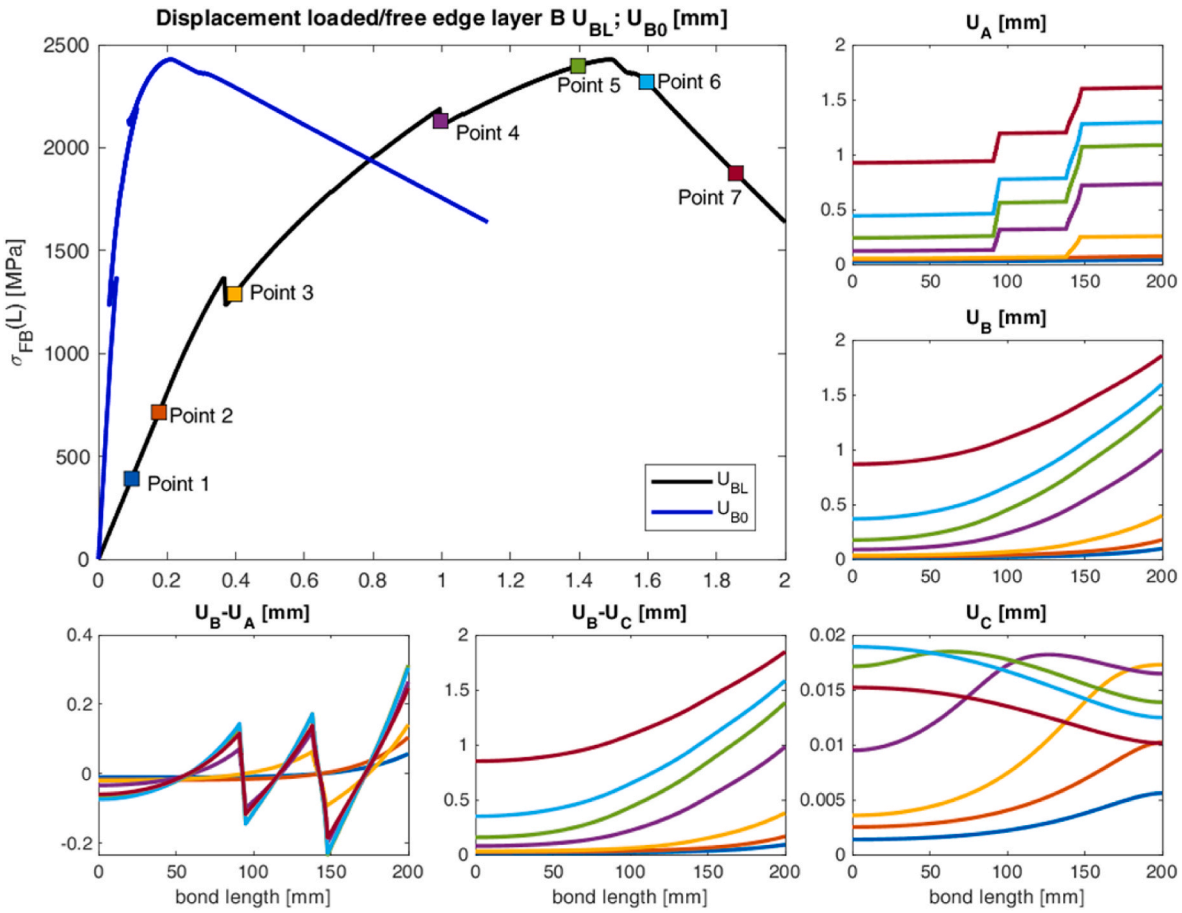

Fig. 14. Ascione et al. (2015) data. From the top-left in clockwise order. Stress $\sigma_{FB}(L)$ - displacements U_{BL}, U_{B0} curves; $U_A, U_B, U_C, U_B - U_C, U_B - U_A$ behavior along the bond length (the color of the curves corresponds to the particular instants investigated during the loading process and match those of the points represented in the top-left sub-figure). (For interpretation of the references to color in this figure legend, the reader is referred to the Web version of this article.)

For the loaded edge, other three equations are written:

$$\begin{aligned}&\mathrm{diag}(0\quad 1\quad 0\quad 1\quad 0\quad 1)\mathbf{Y}^{2n_e-1,k}\left(C_q^{2n_e-1,k},L\right)\\&=\left[0\quad U_{BL}^{2n_e-1,k}\quad 0\quad 0\quad 0\quad 0\right]^T=\mathbf{U}_{BL}^{2n_e-1,k}\end{aligned}\tag{10}$$

Where $U_{BL}^{2n_e-1,k}$ is the displacement applied on the loaded edge of layer B at the time step k.

Leaving out in Eq. (9)(10) the identity equations and considering Eqs. (8)–(10) contemporarily, they constitute a linear system of $12n_e-6$ equations into $12n_e-6$ unknowns, the latter being the $C_q^{j,k}$ (from $j=1$ to $j=2n_e-1$) integration constants of all the elements.

Suitably assembling the previously introduced equations, the problem is reformulated as follows:

$$\mathbf{C}^k\mathbf{K}^k=\mathbf{U}_{BL}^k\tag{11}$$

Where $\mathbf{C}^k$, $\mathbf{K}^k$ and $\mathbf{U}_{BL}^k$ are respectively the assembled vector of the integration constants of all the elements, the assembled square matrix of the coefficients of Eqs. (8)–(10) and the vector of external loads applied at the time step k. It is interesting to notice that $\mathbf{U}_{BL}^k$ is a vector of all zeros exception made for the third last component which is equal to the displacement $U_{BL}^{2n_e-1,k}$, imposed at the loaded edge on layer B.

The model proposed, in its current form, works under displacement control (see for instance Eqs. (10) and (11)). Consequently, it can capture only a softening behavior. On the contrary, to reproduce snap back, an arc-length algorithm should be generally used. However, it is worth mentioning that there is a particular case where a displacement control may allow to see a snap-back of the loaded edge, namely when the displacement is monotonically increased at the free edge.

In this latter case, different boundary conditions should be written, for instance assuming that the displacement imposed is that of layer B at the free edge, $U_{B0}^{1,k}$. In such a case, Eqs. (9) and (10) rewrite as follows:

$$\begin{aligned}&\mathrm{diag}(0\quad 1\quad 0\quad 1\quad 1\quad 1)\mathbf{Y}^{1,k}\left(C_q^{1,k},0\right)=\left[0\quad U_{BL}^{1,k}\quad 0\quad 0\quad 0\quad 0\right]^T\\&\mathrm{diag}(0\quad 0\quad 0\quad 1\quad 0\quad 1)\mathbf{Y}^{2n_e-1,k}\left(C_q^{2n_e-1,k},L\right)=\mathbf{0}_{6\times1}\end{aligned}\tag{12}$$

By means of the imposition of the BCs written in Eq. (12), it is possible to simulate the snap back observed after the attainment of the peak load, which is documented in the literature [39–41].

By the inversion of matrix $\mathbf{K}^k$, $\mathbf{C}^k$ vector is computed through Eq. (11) and finally $\mathbf{Y}^{j,k}$ is derived for each element j via Eq. (8).

The non-linearity of the materials (mortar and interfaces) is dealt with a fully explicit strategy of updating for the elastic moduli/interface stiffness, as schematically represented in Fig. 4.

We distinguish between interfaces on mortar layers and interfaces between mortar and fiber net. In the first case, indeed, σ_{MA} (σ_{MC}) are responsible for strain localization, whereas $\tau_{I,AB}$ ($\tau_{I,CD}$) are not.

In all those elements (or interfaces between superimposed layers within one element) where the non-linearity can activate, at the end of the load step k (which is always elastic), the dependent variables on each node i of the discretization are known solving Eq. (11) and substituting into Eq. (8), namely $\sigma_{MA}^{i,k}$, $\sigma_{MC}^{i,k}$, $\sigma_{FB}^{i,k}$, $U_A^{i,k}$, $U_B^{i,k}$, $\sigma_C^{i,k}$, where the superscript i indicates the node and k the load step.

It is necessary to specify that $\tau_{I,AB}$ ($\tau_{I,CD}$) are discontinuous on node i

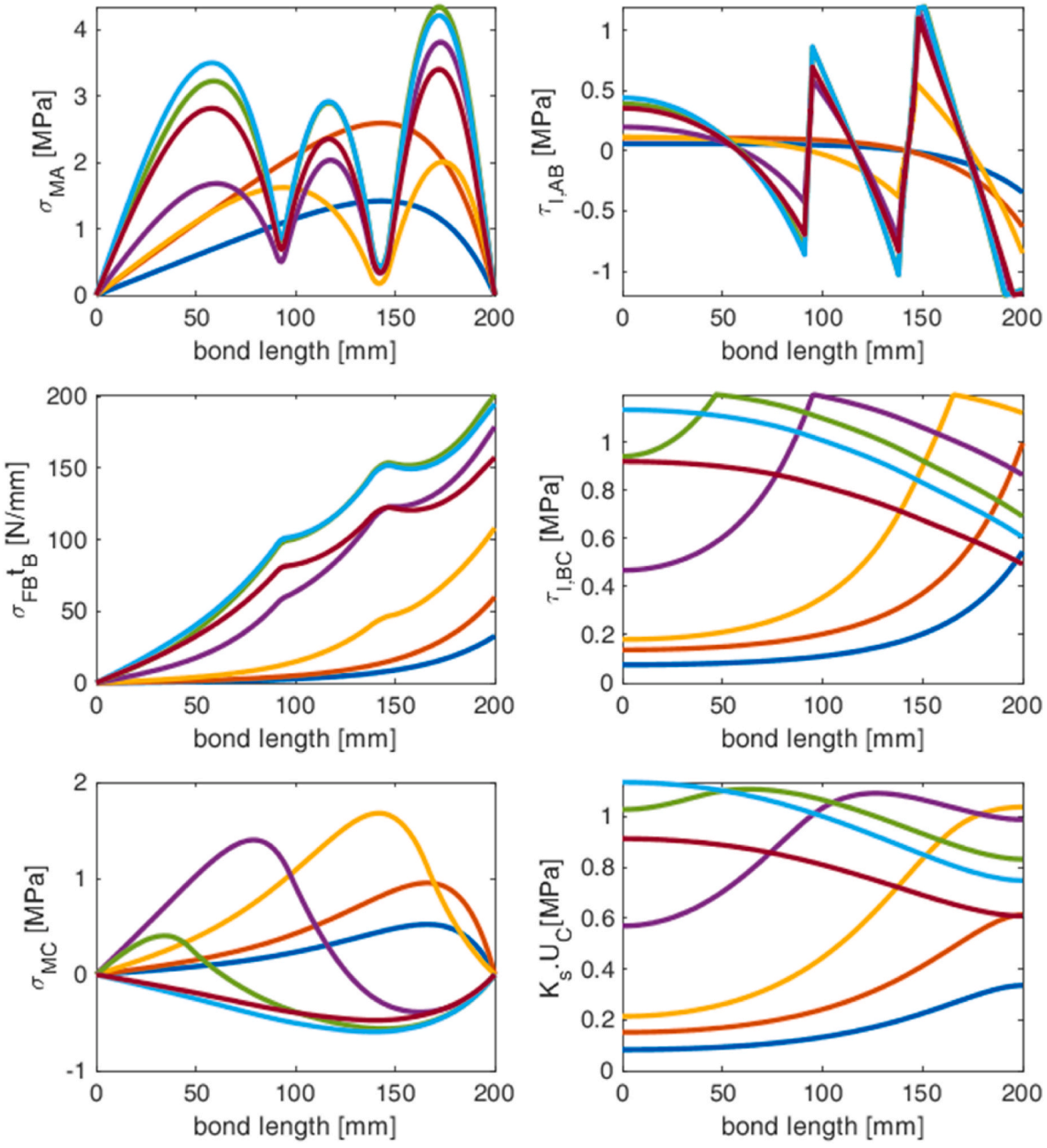

Fig. 15. Ascione et al. (2015) data. From the top-left in clockwise order. $\sigma_{MA}, \tau_{I,AB}, \tau_{I,BC}, K_s U_C, \sigma_{MC}, \sigma_{FB} t_B$ behavior along the bond length (the color of the curves corresponds to the particular instants investigated during the loading process and match those of the points represented in the previous sub-figure); in the simulations, it is assumed $K_s = 10K_I$. (For interpretation of the references to color in this figure legend, the reader is referred to the Web version of this article.)

passing from element $j-1$ to the neighbor element j if the interface stiffness K_I is different between the two elements. The stiffness update of the interface is performed element by element, so considering for the sake of example an interface between layers A & B, an element j and a node i, the shear stress at the end of the load step k is the following:

$$\tau_{I,AB}^{i,j,k} = K_{IAB}^{j,k}\left(U_A^{i,k} - U_B^{i,k}\right) \tag{13}$$

Where $K_{IAB}^{j,k}$ (see Fig. 4) is the stiffness of the interface between A & B within the element j at the load step k.

Let us consider for the sake of simplicity, as already mentioned, a linear softening behavior for the interfaces, characterized by a peak tangential strength equal to c_0, an initial stiffness equal to K_I (so that the slip at the elastic limit is $\Delta_{Ie} = c_0/K_I$) and an ultimate slip equal to Δ_{Iu}.

$\tau_{I,AB}$ varies inside the element according to an exponential law; the stiffness update for the element can be performed according to a certain arbitrary rule that introduces an approximation error which clearly tends to vanish reducing the length of the element. The most straightforward assumption made here is to consider the average stress between the extremes of the element, namely:

$$\tau_{I,AB}^{j,k} = \frac{\tau_{I,AB}^{i,j,k} + \tau_{I,AB}^{i+1,j,k}}{2} \tag{14}$$

$\tau_{I,AB}^{j,k}$ is then projected on the softening stage by means of the following formula:

$$\tau_{I,AB}^{j,k} = \frac{\Delta_{Iu} - \frac{\tau_{I,AB}^{j,k}}{K_{IAB}^{j,k}}}{\Delta_{Iu} - \Delta_{Ie}} c_0 \tag{15}$$

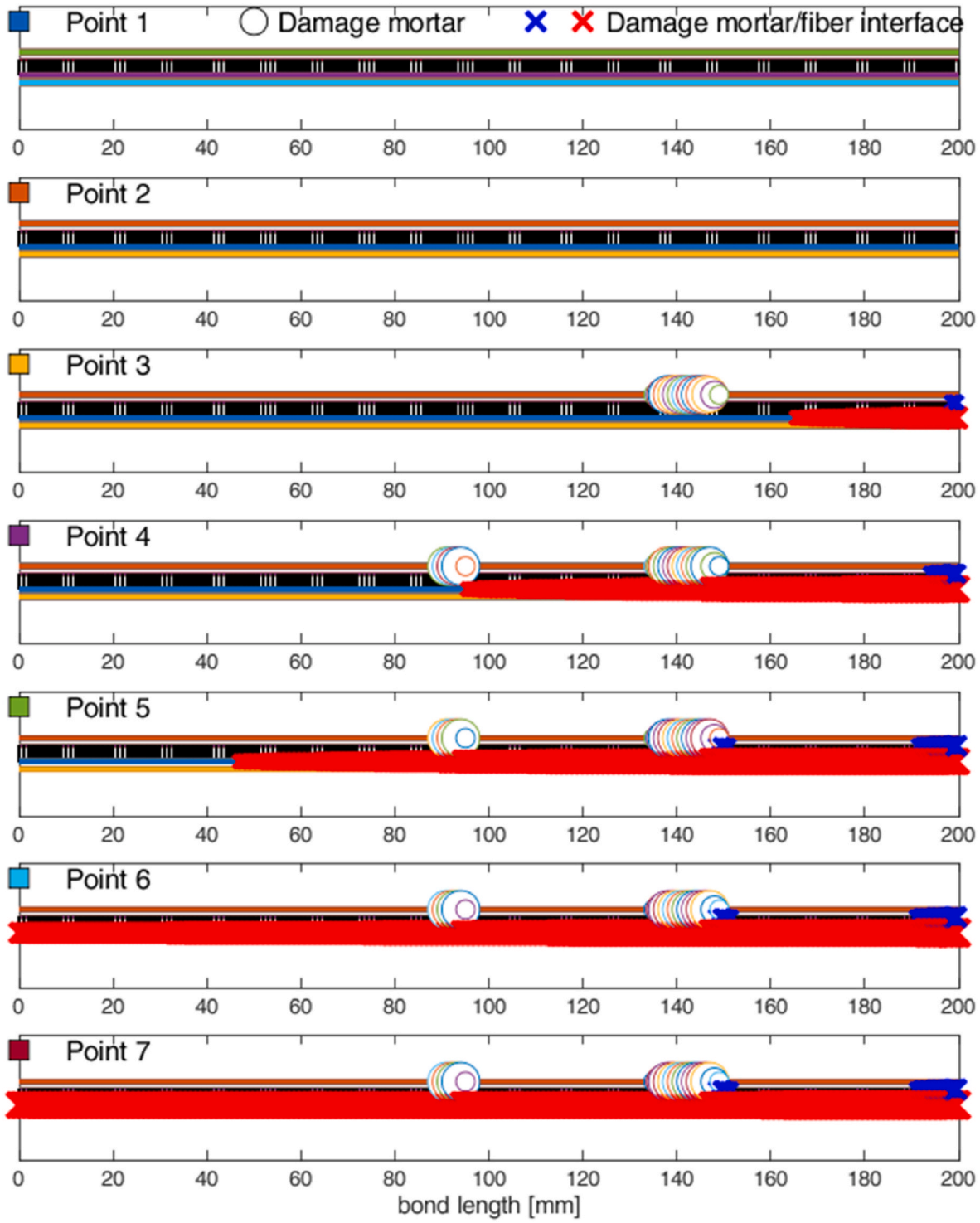

Fig. 16. Ascione et al. (2015) data. Propagation of damage inside mortar layers and interfaces at the different instants investigated during the loading process. White circles and blue/red crosses represent mortar and interface damage, respectively. Their dimension is proportional to the amount of damage. (For interpretation of the references to color in this figure legend, the reader is referred to the Web version of this article.)

Where $\tau'^{j,k}_{I,AB}$ indicates the tangential stress projected on the softening branch at fixed slip $\tau^{j,k}_{I,AB}/K^{j,k}_{IAB}$ and all the other symbols have been already introduced. Having defined $\tau'^{j,k}_{I,AB}$ as per Eq. (15), the stiffness of the interface at the $k+1$ load step is computed as follows:

$$K^{j,k+1}_{IAB} = \frac{\tau'^{j,k}_{I,AB}}{\tau^{j,k}_{I,AB}} K^{j,k}_{IAB} \tag{16}$$

For mortar layers, the procedure is formally identical, so that the elastic modulus of a mortar layer, say A, in the element j is updated in a new load step as follows:

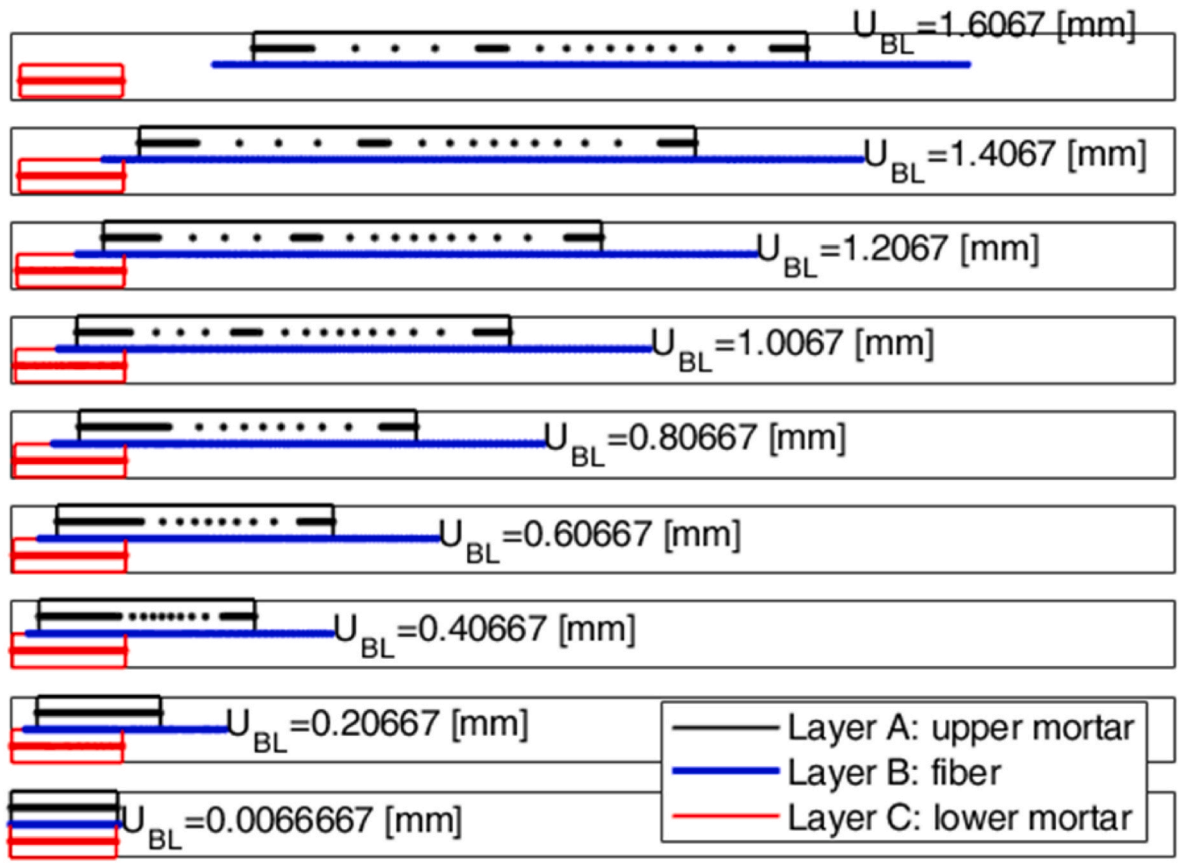

Fig. 17. Ascione et al. (2015) data. Deformed shapes of the reinforcement system. Snapshots taken at nine values of the displacement U_{BL} applied at the loaded edge.

$$E_{MA}^{j,k+1} = \frac{\sigma'^{j,k}_{MA}}{\sigma^{j,k}_{MA}} E^{j,k}_{MA} \tag{17}$$

Where $\sigma^{j,k}_{MA}$ is the average mortar axial stress on element j at the end of step k, $E^{j,k}_{MA}$ is the mortar elastic modulus and $\sigma'^{j,k}_{MA}$ is the projection of $\sigma^{j,k}_{MA}$ on the softening branch at fixed axial strain.

The algorithm implemented to solve the non-linear problem (namely the progressive degradation of the elastic properties, see Eqs. (16) and (17)) has the advantage that is fully explicit, but in principle sub-iterations should be used at the end of each iteration to avoid an inconsistency between updated stresses calculated at the end of the application of the load step and the displacements found considering Eqs. (11) and (7). However, if the imposed load step is sufficiently small, the error tends rapidly to zero and to embed a sub-iteration strategy is not strictly necessary to improve the numerical accuracy. The computational burden remains in any case extremely reduced even using very small load steps, because only a matrix factorization is needed.

Another interesting aspect of the algorithm used that deserves a short discussion is related to the activation of the last phase of the trilinear curves. In practice, when the materials reach the third and last phase, Eqs (16) and (17) would return back null values respectively for the matrix elastic modulus and the interface stiffness. Such values, then inserted in Eq. (6) may be responsible for potential numerical issues, because some elements of the matrix would become indefinite. In particular, problems may arise exclusively as far as the matrix Young's modulus is concerned. Consequently, the update of the elastic modulus when the matrix reaches the last phase of the tri-linear curve is carried out in the current implementation imposing a value not exactly null, but very small (10^{-6} MPa).

A preliminary example to test the performance of the model proposed is hereafter discussed and called Benchmark 0 for the sake of clearness. Data assumed are realistic and represent a slight modification of those used by Milani & Grande in Ref. [46]. In turn, Milani & Grande refer to experimental data provided by Carloni and co-workers in Ref. [7], who carried out single-lap direct-shear tests on a FRCM reinforced concrete block, where the reinforcement system was constituted by one layer of fiber net embedded into two layers of mortar. The failure mode observed was essentially at the matrix-fiber interface; taking inspiration from such observation, Zou et al. [41] had the idea to simplify the complexity of the stress transfer between mortar and fiber and proposed a predicting mortar-fiber interface tri-linear model with softening that in general permits to derive in-closed form the global response in terms of force applied-displacement in rc/masonry elements reinforced with FRCM and subjected to single lap shear tests. Such assumption -by definition and contrarily to the model here proposed-does not allow to have any local insight into what happens in the different components of the reinforcing system, where many elements may behave contemporarily in a non-linear manner.

Here it is worth noting that a comprehensive validation against experimental data available in the literature is postponed to the following Section on purpose, because the present aim is to focus mainly on the numerical aspects of the procedure, which are worthy of deep investigation prior the application on real case-studies. The mechanical properties adopted for mortar and mortar/fiber interface can be retrieved considering Fig. 5, whereas the geometry of the FRCM reinforcement and the elastic modulus of the fiber are provided in Table 1. When comparing with data assumed by Milani & Grande [46], the only parameter that turns out to be different is the mortar tensile strength, here kept equal to 1.5 MPa (i.e. less than that assumed by Milani & Grande in Ref. [46] and equal to 3.5 MPa) because the aim is to show the diffusion of mortar damage in different positions of the bonded length, which in this case occurs contemporarily with the damage of the interface between layers B & C.

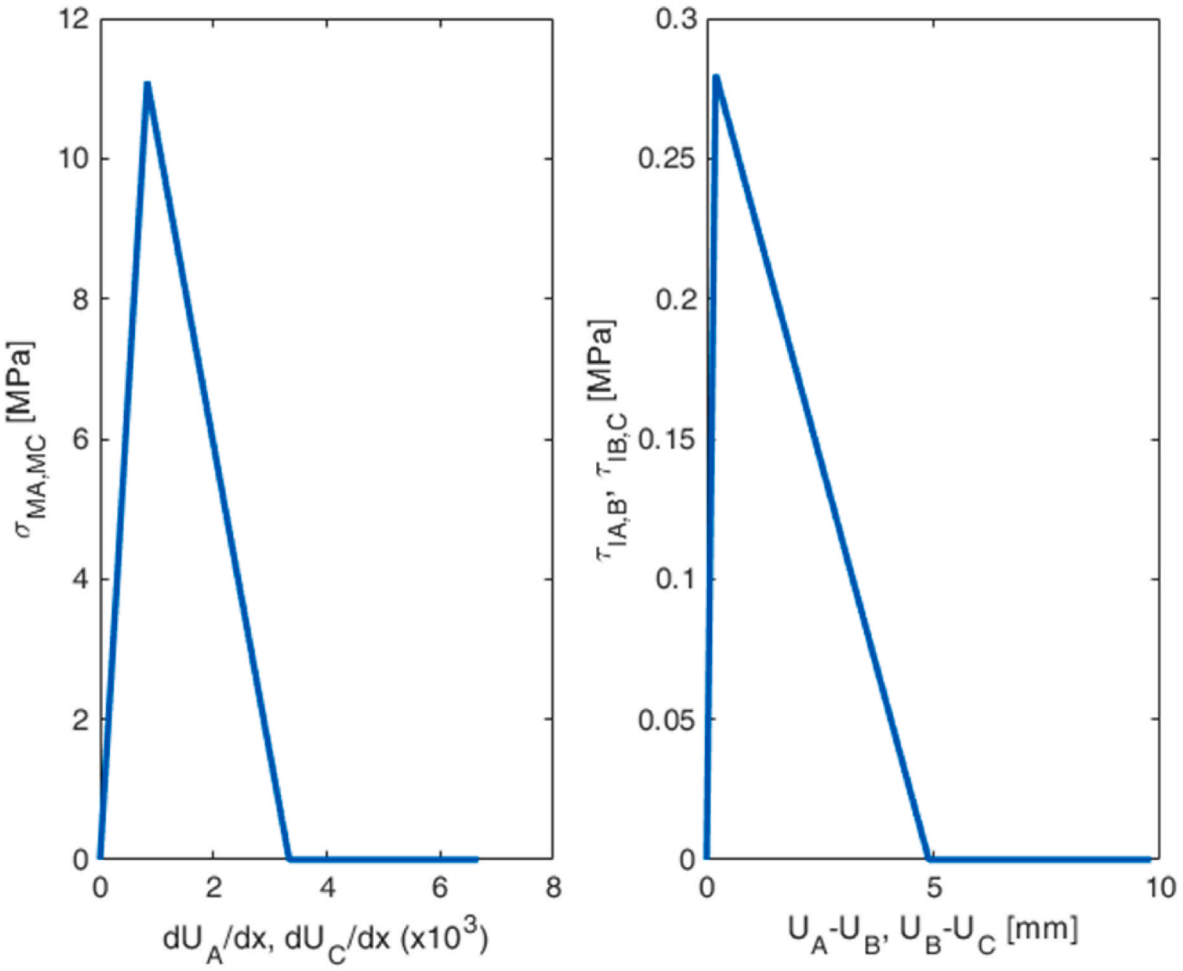

Fig. 18. De Santis et al. (2018) data. Monoaxial stress-strain behavior assumed for mortar layers A & C (left) and shear stress-slip relationship of the interfaces between layers AB & BC (right).

Table 3
De Santis et al. (2018) experimental data. Reinforcement and matrix properties.

Label	reinforcement				matrix			
	type	E_F [MPa]	t_B [mm]	L [mm]	Type	E_M [MPa]	f_{tM} [MPa]	$t_A = t_C$ [mm]
De Santis et al. (2018)	Carbon	242000	0.047	260	Fiber-reinforced polymer modified cementitious mortar	13300	11.1	6.5

Speaking about the modelling parameters, a discretization with $n_e = 70$ is adopted, with length of the mortar elements considered non linear (L_i) set equal to 1 mm. A progressively increased displacement of the fiber net at the loaded edge U_{BL} is imposed in 200 load steps. It is also imposed that $K_s = 100\ K_{IAB}$, a value of stiffness much higher than that of the interfaces. In this way, any possible elastic sliding between layer C and substrate is a-priori excluded, but it will be shown in the following Section that, also decreasing K_s, the sensitivity of the obtained results is in practice very low.

The global response obtained with the aforementioned parameters is depicted in Fig. 6, where on the horizontal and vertical axes, respectively, layer B displacement and fiber stress at the loaded edge are represented. When the substrate is assumed less rigid ($K_s = 10\ K_{IAB}$), see Fig. 7, the global response observed is essentially the same, whereas an unrealistically too low vale ($K_s = 1\ K_{IAB}$) is associated to a more deformable response and a different shape of the force-displacement curve, which typically is a consequence of the triggering of a dissimilar failure mechanism.

Returning back to Fig. 6, it shows also how the kinematic variables relevant for layers A-C (displacements) and interface between them (slips) vary along the FRCM length during the numerical analyses. Nine instants are analyzed in detail, identifying them with square markers filled with different colors. Marker colors correspond to those of the curves representing the internal variables.

Looking also at the trend of static variables (normal stresses acting inside the layers and shear stresses at the interface between them) represented in Fig. 8, it can be deduced that the debonding proceeds for the progressive damage of the interface between fiber and inner mortar layer, with the formation of three localized cracks in layer A.

The numerical results shown in Fig. 8 suggest also that (a) the normal stresses in the central layer B could attain quite high values, which could approach the yield/rupture stress, and (b) at least at some levels of prescribed displacement, the inner mortar layer passes from compression to tension along the bonded length, implying flexure of the strengthening system. Whilst the first issue can be easily managed removing the linear elastic hypothesis for layer B, the latter is outside the possibilities of the model proposed, because a fully 2D approach should be used.

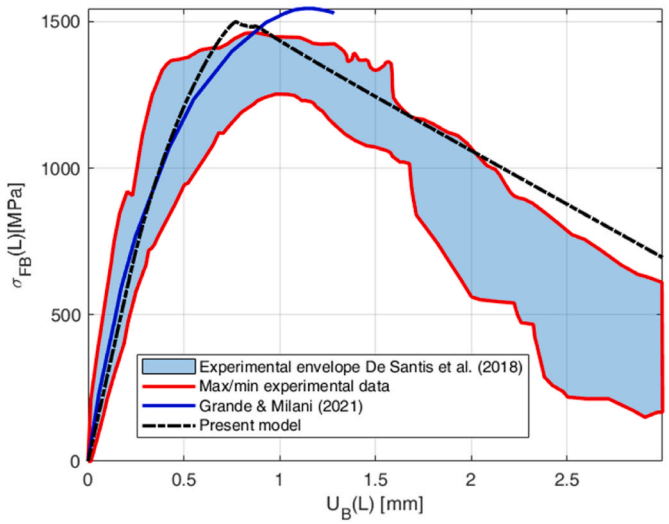

Fig. 19. De Santis et al. (2018) data. Global behavior. Comparison among present model, numerical curve obtained by Grande & Milani [45] and experimental data envelope.

As it can be deduced from Fig. 9, outer mortar cracks first at about 175 mm from the loaded edge and far before the interface between layers B & C enters in the non-linear stage. The crack band -about 70 mm long-remains stable until the end of the simulations. Between Points 3 and 6, at the interface BC damage propagates with a front moving from the right to the left up to the mortar cracked band. Then other two bands of crack appear in the upper mortar layer, one at 160 mm from the free edge and the other near the loaded edge, where the interface is already almost fully debonded. Contemporarily, the BC interface damage front continues to move towards the free edge. A further interesting insight into the previously mentioned features of the evolution of damage is also provided in Fig. 10, where the deformed shapes obtained at the different instants are depicted magnifying suitably the displacements for the sake of clearness.

In general, considering together Figs. 9 and 10, it can be deduced that the zones where cracks tend to form and localize may be detected only in an approximate way, in the sense that only relatively large regions of the outer layer undergoing damages are identified. The exact location of the cracks, on the contrary, depends numerically on the refinement of the mesh used. Experiments show macroscopically a promising agreement with the numerical prediction, but a further insight would be necessary to propose a model more powerful in this regard. Typically, the crack spacing, localization, or distribution are commonly attributed to the bond characteristics, which reflect in the model through the properties assigned to the interfaces. Such investigation would require first of all a sound experimental base, which is quite difficult to carry out for FRCM using standard techniques effective in other cases, because the interfaces playing a major role in the phenomenon are located deep inside the thickness of the reinforcing system.

Having an insight into the role played by the space and time discretization, further numerical analyses are carried out, keeping first the time discretization constant (200 step) and assuming $n_e = 35$ (inter-

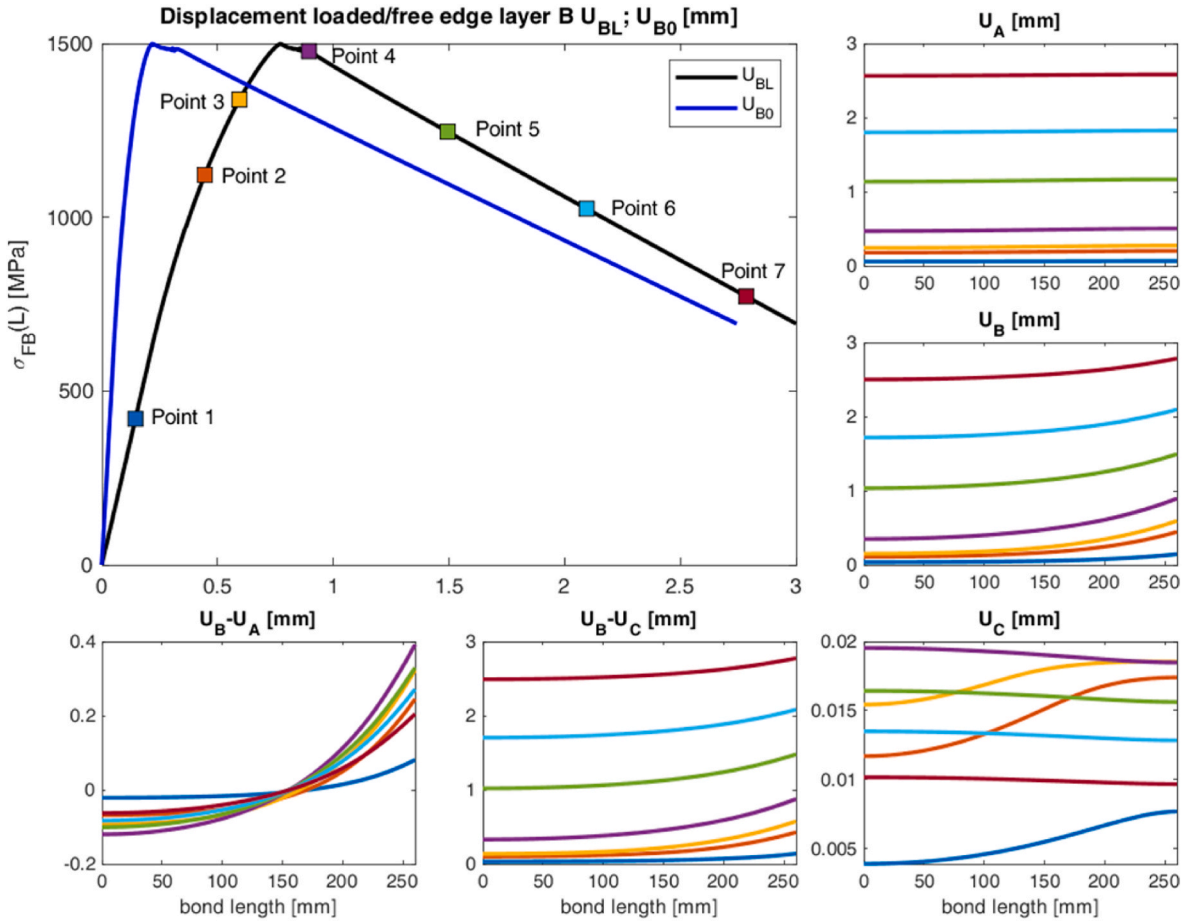

Fig. 20. De Santis et al. (2018) data. From the top-left in clockwise order. Stress $\sigma_{FB}(L)$ - displacements U_{BL}, U_{B0} curves; $U_A, U_B, U_C, U_B - U_C, U_B - U_A$ behavior along the bond length (the color of the curves corresponds to the particular instants investigated during the loading process and match those of the points represented in the top-left sub-figure). (For interpretation of the references to color in this figure legend, the reader is referred to the Web version of this article.)

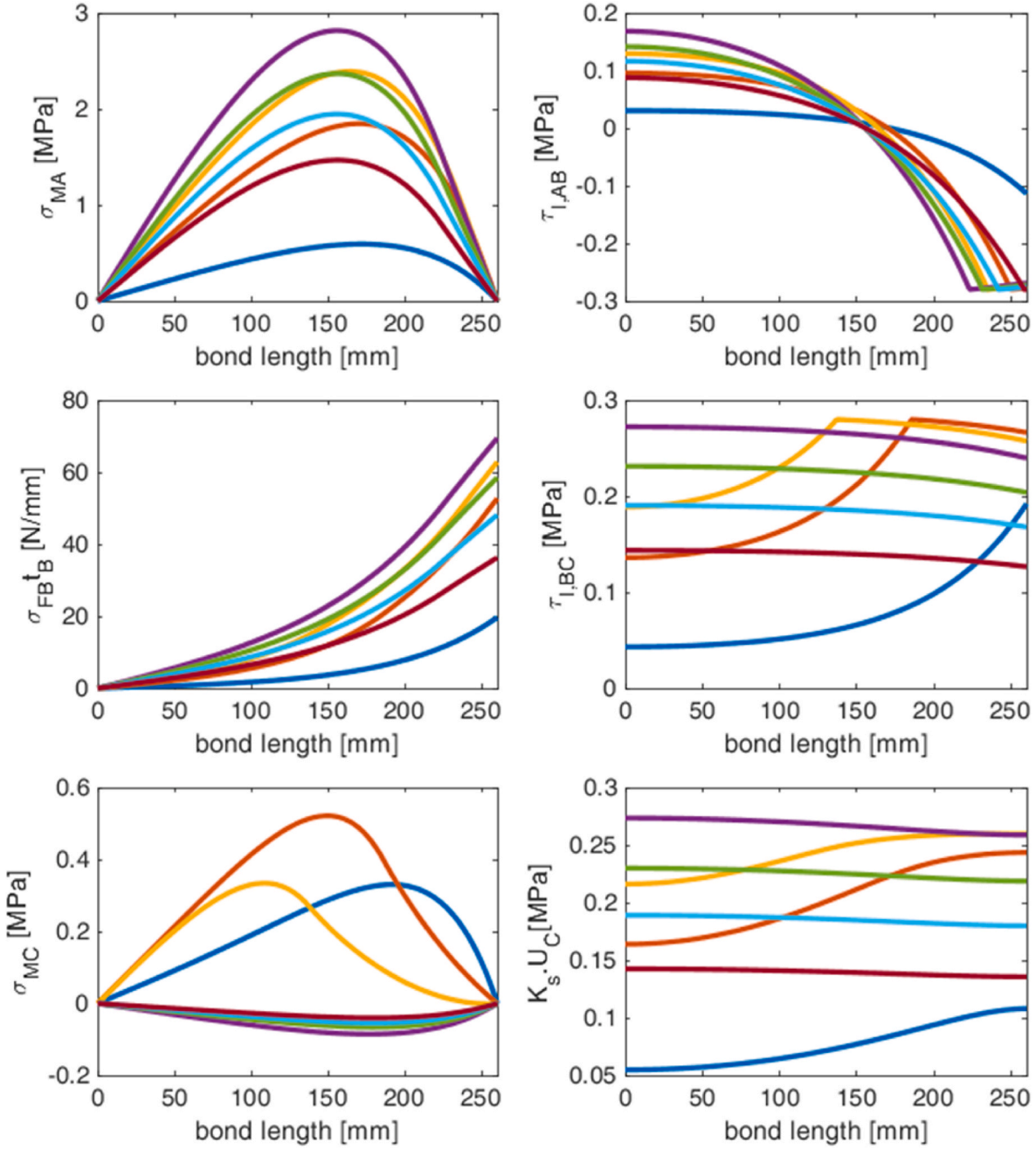

Fig. 21. De Santis et al. (2018) data. From the top-left in clockwise order. $\sigma_{MA}, \tau_{I,AB}, \tau_{I,BC}, K_s U_C, \sigma_{MC}, \sigma_{FB} t_B$ behavior along the bond length (the color of the curves corresponds to the particular instants investigated during the loading process and match those of the points represented in the previous sub-figure); in the simulations, it is assumed $K_s = 10K_I$. (For interpretation of the references to color in this figure legend, the reader is referred to the Web version of this article.)

mediate mesh) and $n_e = 7$ (rough mesh). The results obtained (global response) are depicted in Fig. 11-a. As it is possible to notice, even with a very unrefined mesh, converged results are obtained. Obviously if the aim is to have a precise insight into the local behavior of the different parts of the reinforcement, the utilization of a reasonably large number of elements is recommended. Similar considerations can be repeated decreasing the load steps, as shown in Fig. 11-b, where, keeping $n_e = 35$, results obtained with 100 and 50 steps are reported.

3. Applications and comparison with experimental evidence

The present section applies the numerical model proposed on two experimentally tested case studies collected from the literature. They rely in shear-lap bond tests carried out on Textile Reinforced Mortar TRM specimens manufactured with different materials (reinforcement and matrix), geometrical configuration and applied on masonry/brick substrates. The same experimental data (among others) were considered by Grande & Milani to investigate the accuracy of their interface model, see Ref. [45] for details.

3.1. Validation against experimental data by Ascione et al. (2015)

The first validation is carried out against some experimental results provided in Ref. [8] by Ascione and co-workers. Hereafter, the considered experimental data are labeled as Ascione et al. (2015) for the sake of clarity. Single lap shear tests were carried out on a Steel Reinforced Grout SRG strengthening system applied on a tuff block substrate. The SRG is constituted by a unidirectional textile made by galvanized Ultra

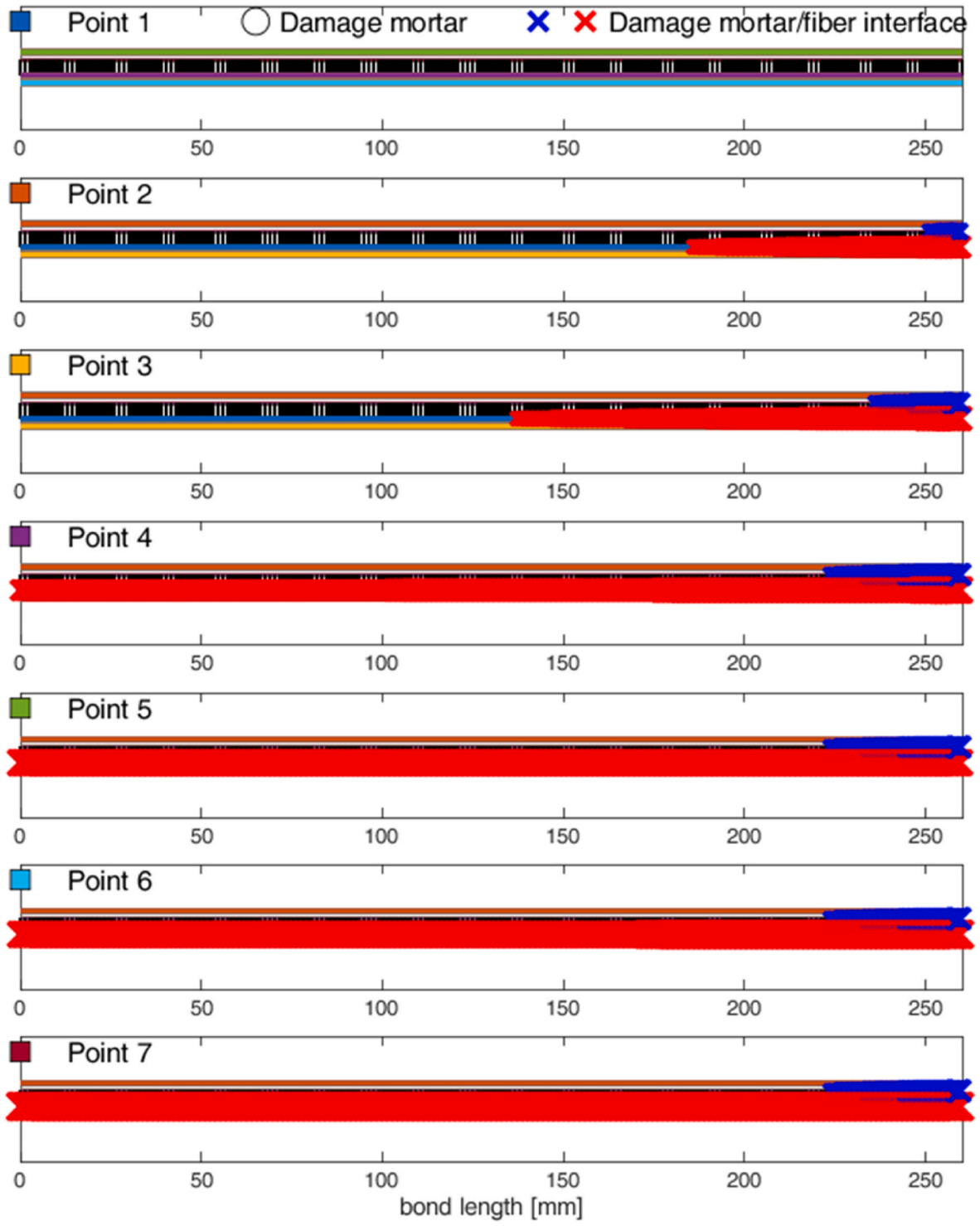

Fig. 22. De Santis et al. (2018) data. Propagation of damage inside mortar layers and interfaces at the different instants investigated during the loading process. White circles and blue/red crosses represent mortar and interface damage, respectively. Their dimension is proportional to the amount of damage. (For interpretation of the references to color in this figure legend, the reader is referred to the Web version of this article.)

High Tensile Strength Steel UHTSS cords embedded into a double layer of a mineral/natural hydraulic lime mortar. Table 2 summarizes the main characteristics (geometrical and mechanical) of the reinforcement system, provided in Ref. [8]. For this type of specimens, the authors mainly observed a failure mode characterized by the debonding at the textile/matrix interface.

No information is provided for the interface properties, because a complex experimental equipment -for instance based on fiber optic wires, as proposed in Ref. [20], would be required. In the present simulations, the properties adopted by Grande & Milani [45] are slightly modified to fit better experimental data. In particular, it is worth mentioning that Grande & Milani [45] used different properties of the upper and lower interface, strictly connected to the specificity of their model rather than based on experimental data, which in any case are impossible to achieve contemporarily.

The uniaxial stress-strain behavior adopted for the mortar layers and

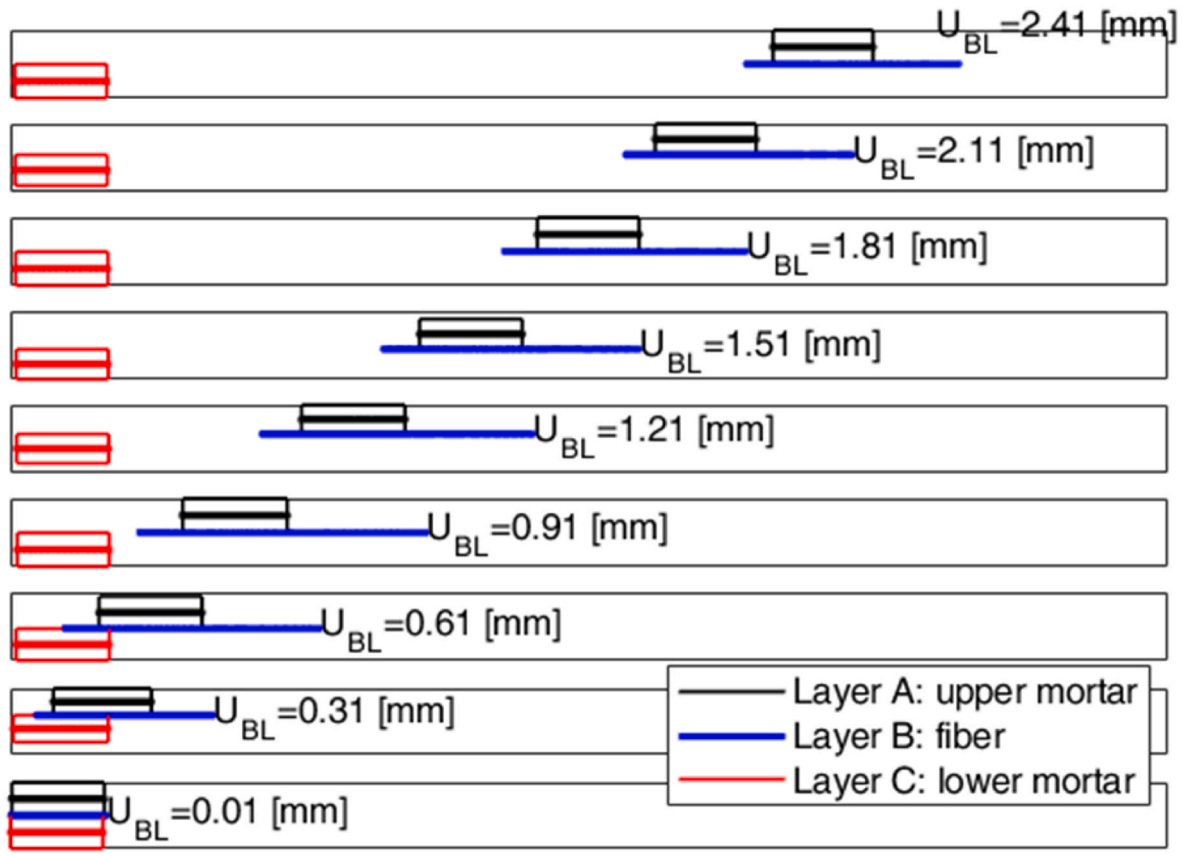

Fig. 23. De Santis et al. (2018) data. Deformed shapes of the reinforcement system. Snapshots taken at nine values of the displacement U_{BL} applied at the loaded edge.

the shear stress-slip relationship used for the interfaces are reported in Fig. 12. K_s is assumed ten times higher than the value assumed for $K_{IAB} = K_{IBC}$.

Using a discretization with $n_e = 200$, assuming $L_i = 10^{-4}L$ and 600 load steps (under a displacement based control strategy with an applied fiber displacement U_{BL} at the loaded edge), the global response depicted in Fig. 13 is obtained, where also the envelope of the experimental results and the curve obtained by Grande & Milani [45] are reported. With reference to Fig. 13, on the horizontal axis the fiber displacement at the loaded edge is represented, whereas the vertical axis corresponds to the fiber stress, again calculated at the loaded edge.

As it can be noted, the agreement with Grande & Milani [45] numerical results can be considered in any case satisfactory. When compared with Grande & Milani [45] model, the present approach has the advantage of providing a precise local information regarding the propagation of the non-linearity in the different layers.

The numerically obtained results are also in very good agreement with experimental data, falling within the experimental envelope almost everywhere and with a global and local predictivity of the physical phenomena progressively occurring in the reinforcing system much better than that exhibited by the state of the art in the field.

Figs. 14 and 15 show how the internal variables (kinematic and static respectively) vary along the bond length, at different meaningful instants of the loading process; such instants are identified in the global load-displacement curves with square symbols filled with different colors. The curves representing the internal variables are plotted with the same colors to facilitate the reading of the results obtained.

The first two instants represented (Point 1 and Point 2) are elastic, whereas in Point 3 the upper and lower interfaces start to behave inelastically in a short portion near the loaded edge. Noticeable is the damage of the upper interface (blue crosses). Immediately before Point 3, a drop of the load carrying capacity is visible in the global curve, see Fig. 14, because the upper mortar layer starts to crack. The front of damage in the inner interface, see Fig. 16, continues to move towards the free edge, the normal stress distribution in the upper mortar layer changes for the formation of another crack band (Point 4) and the stress in the fiber continues to grow, because the reinforcement still has additional resources to spend in all that portion between the free edge and the cracked sections of the upper mortar layer. Obviously, the stiffness decreases if compared with that of the elastic stage, but still remains considerably high. Two major drops of the load carrying capacity are visible in the global load-displacement curve of Fig. 14, corresponding to the aforementioned physical phenomenon, i.e. the formation of new cracks in the external mortar layer. The location of the second crack is obviously shifted towards the free edge.

Such conclusions can be easily verified looking either at the map of damages present at the different instants investigated and represented in Fig. 16, or by considering contemporarily the distribution of normal stresses in the upper mortar layer and the shear stress at the lower/upper interfaces. The jumps visible in the mortar upper layer displacement provided in Fig. 14 gives a precise information of the actual position of the cracks forming. Point 7 corresponds roughly to the specimen failure. The inner interface is almost completely in the inelastic stage and the upper mortar layer exhibits two concentrated crack bands along the bond length. The deformed shapes of the reinforcement system, depicted at nine different instants of the loading process, are provided in Fig. 17. The snapshots reported in Fig. 17 furnish an immediate idea of the progression of damage in the different layers. The mode of failure observed experimentally (i.e. a slippage of the steel grid from the inner mortar) is clearly visible also in the numerical model; interestingly to notice, the approach proposed is able to reproduce the contemporary cracking of the outer mortar layer and also the limited damage of the

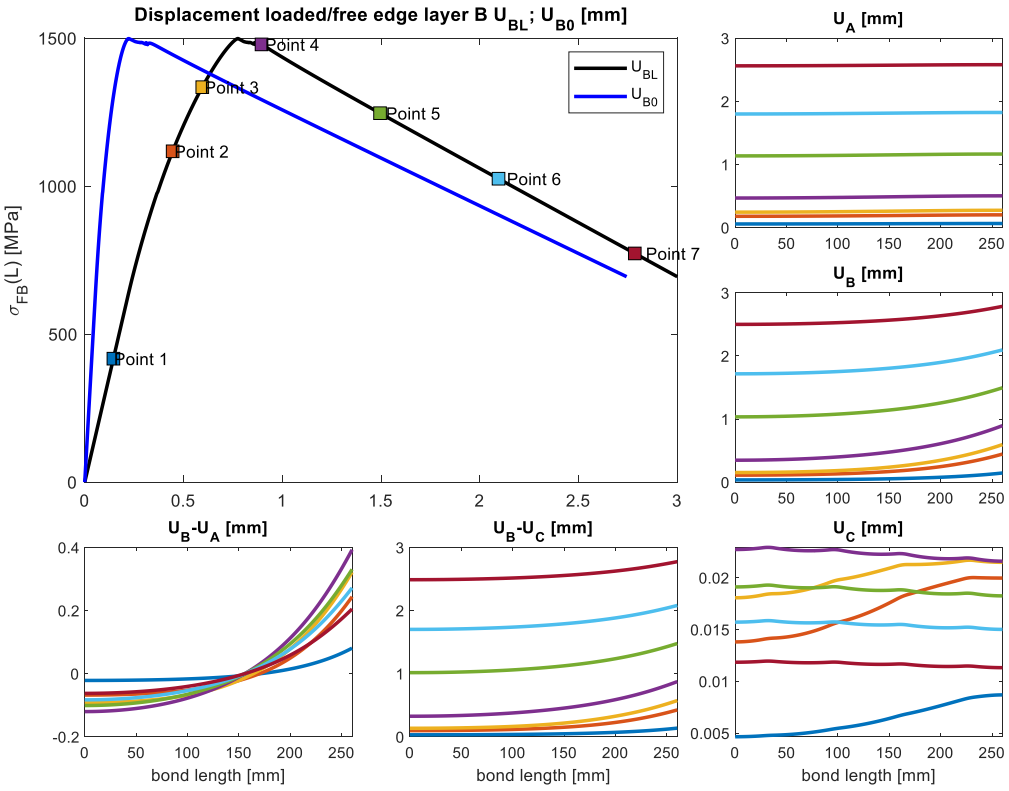

Fig. 24. De Santis et al. (2018) data, investigation in presence of realistic values of stiffness for the substrate (masonry). From the top-left in clockwise order. Stress $\sigma_{FB}(L)$ - displacements U_{BL}, U_{B0} curves; $U_A, U_B, U_C, U_B - U_C, U_B - U_A$ behavior along the bond length (the color of the curves corresponds to the particular instants investigated during the loading process and match those of the points represented in the top-left sub-figure). (For interpretation of the references to color in this figure legend, the reader is referred to the Web version of this article.)

interface between layer A and B. Fig. 17 shows also that the assumed value of the stiffness between layer C and substrate K_s has little influence, but a perceivable elastic sliding is present.

3.2. Validation against experimental data by De Santis et al. (2018)

The last validation of the model is done with reference to some experimental data provided by De Santis et al. in Ref. [12]. In particular, among the variety of experimental results presented, those relative to a set of FRCM-to-substrate shear bond tests characterized by a FRCM reinforcement made of a balanced carbon fabric embedded into a cementitious polymer modified mortar reinforced with short fiber whiskers is considered. The substrate is constituted by a masonry pillar with 5 standard Italian bricks (heigh: 55 mm) and 10 mm thick mortar joints.

The mechanical properties of the matrix, of the fiber and of the interfaces with the geometric characteristics of the different layers are shown in Fig. 18 and collected in Table 3.

Numerical simulations are carried out using a discretization with $n_e = 200$, imposing $L_i = 10^{-4}L$ and progressively applying a displacement U_{BL} to the fiber layer at the loaded edge.

The predictivity of the model is shown in Fig. 19, where the stress-displacement curves at the loaded fiber edge are compared with both the experimental envelope and the numerical response provided by Grande & Milani [45]. As it is possible to notice, the model is almost always inside the experimental envelope, showing particularly promising stability also in presence of strong softening of the specimen.

Investigating the local behavior in Figs. 20–23, it can be seen that the mode of failure involves almost exclusively the inner interface between layers B & C. Little damage is visible in the outer interface near the loaded edge. This is not surprising, because the mortar used for the matrix exhibits a particularly high strength. Such feature is the main reason that gives to the global curve a particularly smooth appearance. Differently from the previous cases, no steps of the load carrying capacity are visible, which are always a consequence of the formation of cracks inside mortar layers.

Using the same model proposed, an interesting additional insight can be gained investigating the role played by the values of stiffness K_s imposed at the interface between the substrate and the inner matrix layer. In particular, the present comparison deals with small, reinforced masonry pillars built stacking 5 bricks with 4 mortar joints, whose actual reduced stiffness may reflect into a modification of the internal state of stress.

The deformability of the substrate can be simulated assuming for the stiffness K_s values that are directly deducible from the elastic properties of the bricks and the joints. If both materials behave elastically (the study of the non-linearity of the substrate is postponed to a future dedicated research, see a similar investigation for FRP already available in Ref. [50]), the substrate actual stiffness can be lumped at the S interface making the hypothesis that bricks and mortar are subjected to pure shear. Consequently, under such hypothesis, K_s assumes distinct values in correspondence of mortar joints and bricks.

In particular, it is reasonable to assume for both joints (j) and blocks (b) $K_{sj,b} = G_{j,b}/H_b$, where $G_{j,b}$ is the shear modulus, H_b is the effective pillar height and the subscripts j and b refer respectively to joints and blocks. Making the very simplistic hypothesis that $H_b = 250$ mm, and for the sake of comparison with previous results that $K_{s,b} = 10K_{IBC} = 14$ MPa/mm, the shear modulus of the blocks would be $G_b = 3500$ MPa, and the elastic modulus (assuming a Poisson's ratio equal to 0.2) $E_b = 8400$ MPa, which is a numerical value fully realistic for

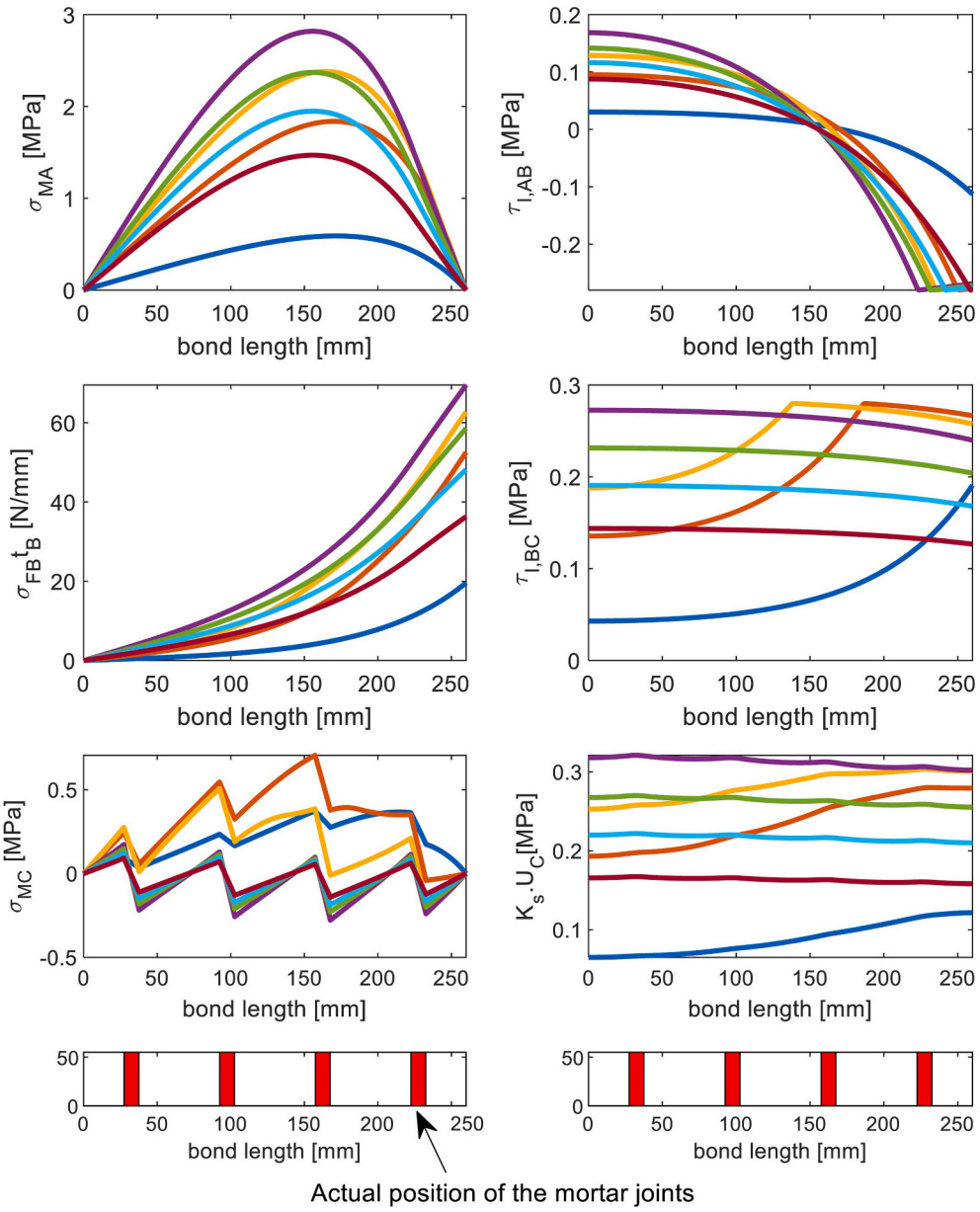

Fig. 25. De Santis et al. (2018) data, investigation in presence of realistic values of stiffness for the substrate (masonry). From the top-left in clockwise order. $\sigma_{MA}, \tau_{I,AB}, \tau_{I,BC}, K_s U_C, \sigma_{MC}, \sigma_{FB} t_B$ behavior along the bond length (the color of the curves corresponds to the particular instants investigated during the loading process and match those of the points represented in the previous subfigure); in the simulations, it is assumed $K_s = 10K_I$. (For interpretation of the references to color in this figure legend, the reader is referred to the Web version of this article.)

common clay bricks. Imposing that $E_j = \frac{1}{10}E_b$, it is possible to have a preliminary insight into the role played by a substrate where the joints are weak.

Again, the elastic modulus of the joint appears quite realistic, especially because mortar may start to crack early under such kind of tests and also because typically the Young's modulus of the joints is sensibly lower than that of the blocks.

The results obtained are shown in Figs. 24 and 25. Such figures should be compared respectively with Figs. 20 and 21. The global behavior, compare Figs. 24 and 20, does not show perceivable differences, whereas as far as the local behavior is concerned, layer C exhibits clear stress jumps (due to the deformable joints, see Fig. 21 where the position of the joints is clearly indicated) and a non-smooth layout for the displacement field U_C, see Fig. 25.

4. Conclusions

A quasi-analytical model to analyze the local behavior of FRCM-to substrate shear bond tests has been proposed. The strengthening system has been considered constituted by three separate and superimposed layers, namely the fiber grid embedded into an upper and lower matrix. Fiber has been assumed elastic, whereas the inorganic matrix layers have been modeled taking into account a linear elastic relationship followed by a softening phase. The three components of the reinforcing system (matrix upper and lower layers and fiber) have been assumed in a monoaxial state of stress, interacting mutually by means of interfaces subjected exclusively to shear stresses and characterized by a tri-linear with softening shear stress-slip relationship. The kinematic and static internal variables are the axial displacements and the normal stresses of the layers, respectively. The lower matrix has been finally connected to the substrate with a further elastic interface. Under such assumptions, a system of first order non linear differential equations has been derived and subsequently solved in quasi-closed form. Two experimental datasets from the literature have been taken into account to estimate the accuracy of the model proposed, which showed an excellent predictivity in reproducing both the global and local behavior.

Future developments of the model discussed should move towards the analysis of curved masonry elements reinforced with FRCM, still a topic largely under investigated. A direct implementation of a novel FE

is expected straightforward and could represent a valid alternative to the utilization of standard approaches nowadays available in the literature to study entire reinforced structural elements, with particular regard to masonry arches and vaults. In such cases, indeed, a crucial coupling between normal and shear internal actions at the interface between strengthening system and support could be responsible for a mechanical behavior quite different from that predicted in a standard debonding test carried out on flat supports. Finally, a straightforward -albeit simplified- evolution of the proposed model can be achieved through the introduction of induced strain in the substrate as external stimulus for debonding.

CRediT author statement

G. Milani: Conceptualization, Methodology, Investigation, Validation, Data curation, Writing- Original draft preparation.

Declaration of competing interest

The authors declare that they have no known competing financial interests or personal relationships that could have appeared to influence the work reported in this paper.

Data availability

Data will be made available on request.

References

[1] Papanicolaou CG, Triantafillou TC, Karlos K, Papathanasiou M. Textile-reinforced mortar (TRM) versus FRP as strengthening material of URM walls: in-plane cyclic loading. Mater Struct 2007;40:1081–97. https://doi.org/10.1617/s11527-006-9207-8.

[2] Toutanji H, Deng Y. Comparison between organic and inorganic matrices for RC beams strengthened with carbon fiber sheets. J Compos Construct 2007;11(5):507–13.

[3] Nanni A. A new tool for concrete and masonry repair – strengthening with fiber-reinforced cementitious matrix composites. Concr Int 2012;34:43–9.

[4] de Felice G, De Santis S, Garmendia L, Ghiassi B, Larrinaga P, Lourenço PB, et al. Mortar-based systems for externally bonded strengthening of masonry. Mater Struct 2014;47(12):2021–37.

[5] Ghiassi B. Mechanics and durability of lime-based textile reinforced mortars. RILEM Technical Letters 2019;4:130–7. https://doi.org/10.21809/rilemtechlett.2019.99.

[6] D'Ambrisi A, Feo L, Focacci F. Experimental analysis on bond between PBO FRCM strengthening materials and concrete. Compos Part B-Eng 2013;44(1):524–32.

[7] Carloni C, D'Antino T, Sneed LH, Pellegrino C. Role of the matrix layers in the stress-transfer mechanism of FRCM composites bonded to a concrete substrate. J Eng Mech 2014;141(6):#04014165.

[8] Ascione L, de Felice G, De Santis S. A qualification method for externally bonded Fibre Reinforced Cementitious Matrix (FRCM) strengthening systems. Composites Part B 2015;78:497–506.

[9] D'Antino T, Sneed LH, Carloni C, Pellegrino C. Influence of the substrate characteristics on the bond behavior of PBO FRCM-concrete joints. Construct Build Mater 2015;101:838–50.

[10] De Santis S, Ceroni F, de Felice G, Fagone M, Ghiassi B, Kwiecień A, et al. Round robin test on tensile and bond behaviour of steel reinforced Grout systems. Compos B Eng 2017;127:100–20. https://doi.org/10.1016/j.compositesb.2017.03.052.

[11] Marcari G, Basili M, Vestroni F. Experimental investigation of tuff masonry panels reinforced with surface bonded basalt textile-reinforced mortar. Compos B Eng 2017;108:131–42.

[12] De Santis S, Hadad HA, De Caso y Basalo F, de Felice G, Nanni A. Acceptance criteria for tensile characterization of fabric-reinforced cementitious matrix systems for concrete and masonry repair. J Compos Construct 2018;22(6):04018048. https://doi.org/10.1061/(ASCE)CC.1943-5614.0000886.

[13] Dalalbashi A, Ghiassi B, Oliveira DV. Textile-to-mortar bond behaviour in lime-based textile reinforced mortars. Construct Build Mater 2019;227. https://doi.org/10.1016/j.conbuildmat.2019.116682.

[14] Ombres L, Mancuso N, Mazzuca S, Verre S. Bond between carbon fabric-reinforced cementitious matrix and masonry substrate. J Mater Civ Eng 2019;31:04018356. https://doi.org/10.1061/(ASCE)MT.1943-5533.0002561.

[15] Crisci G, Ramaglia G, Lignola GP, Fabbrocino F, Prota A. Effects of the mortar matrix on the flexural capacity of masonry cross sections strengthened with FRCM materials. Appl Sci 2020;10(21):1–15. #7908.

[16] Bellini A, Incerti A, Bovo M, Mazzotti C. Effectiveness of FRCM reinforcement applied to masonry walls subject to axial force and out-of-plane loads evaluated by experimental and numerical studies. Int J Architect Herit 2018;12(3):376–94.

[17] Grande E, Fagone M, Rotunno T, Milani G. Modeling of shear-lap tests of flat and curved masonry specimens strengthened by FRCM. Structures 2023;52:437–48. https://doi.org/10.1016/j.istruc.2023.04.014.

[18] Calabrese AS, Colombi P, D'antino T. A bending test set-up for the investigation of the bond properties of FRCM strengthenings applied to masonry substrates. Key Eng Mater 219; 817: 149-157..

[19] Ghiassi B, Xavier J, Oliveira DV, Lourenço PB. Application of digital image correlation in investigating the bond between FRP and masonry. Compos Struct 2013;106:340–9. https://doi.org/10.1016/j.compstruct.2013.06.024.

[20] Bertolesi E, Fagone M, Rotunno T, Grande E, Milani G. Experimental characterization of the textile-to-mortar bond through distributed optical sensors. Construct Build Mater 2022;326:126640. https://doi.org/10.1016/j.conbuildmat.2022.126640.

[21] Grande E, Milani G, Sacco E. Modelling and analysis of FRP-strengthened masonry panels. Eng Struct 2008;30(7):1842–60.

[22] Grande E, Imbimbo M, Sacco E. Simple model for the bond behavior of masonry elements strengthened with FRP. J Compos Construct 2011;15(3):354–63.

[23] Grande E, Imbimbo M, Sacco E. Bond behaviour of CFRP laminates glued on clay bricks: experimental and numerical study. Compos B Eng 2011;42(2):330–40.

[24] Carrara P, Ferretti D. A finite-difference model with mixed interface laws for shear tests of FRP plates bonded to concrete. Compos B Eng 2013;54:329–42. https://doi.org/10.1016/j.compositesb.2013.05.030.

[25] Ceroni F, de Felice G, Grande E, Malena M, Mazzotti C, Murgo F, et al. Analytical and numerical modeling of composite-to-brick bond. Mater Struct 2014;47:1987–2003. https://doi.org/10.1617/s11527-014-0382-8.

[26] Biscaia HC, Chastre C, Silva MAG. Bond-slip model for FRP-to-concrete bonded joints under external compression. Compos B Eng 2015;80:246–59. https://doi.org/10.1016/j.compositesb.2015.06.004.

[27] Grande E, Imbimbo M. A simple 1D-Finite Element approach for the study of the bond behavior of masonry elements strengthened by FRP. Compos B Eng 2016;91:548–58. https://doi.org/10.1016/j.compositesb.2016.02.005.

[28] Grande E, Fagone M, Rotunno T, Bertolesi E, Milani G. Coupled interface-based modelling approach for the numerical analysis of curved masonry specimens strengthened by CFRP. Compos Struct 2018;200:498–506.

[29] Milani G, Fagone M, Rotunno T, Grande E, Bertolesi E. Development of an interface numerical model for C-FRPs applied on flat and curved masonry pillars. Compos Struct 2020;241:112074. https://doi.org/10.1016/j.compstruct.2020.112074.

[30] Martinelli E. Closed-form solution procedure for simulating debonding in FRP strips glued to a generic substrate material. Fibers 2021;9:22. https://doi.org/10.3390/fib9040022.

[31] Bertolesi E, Grande E, Fagone M, Milani G, Rotunno T. Mechanical model based on a BVP for FRPs applied on flat and curved masonry pillars with anchor spikes. Compos Struct 2021;273:114251. https://doi.org/10.1016/j.compstruct.2021.114251.

[32] Zhang D, Yang J, Chi LY. The bond-slip relationship at FRP-to-brick interfaces under dynamic loading. Materials 2021;14:545. https://doi.org/10.3390/ma14030545.

[33] Milani G. Simple model with in-parallel elasto-fragile trusses to characterize debonding on FRP-reinforced flat substrates. Compos Struct 2022;296:115874. https://doi.org/10.1016/j.compstruct.2022.115874.

[34] Capozucca R, Ernesto G, Milani G, Bertolesi E. Fully analytical model for the analysis of externally bonded composites applied to brittle supports: sensitivity analysis. Int J Magn Reson Imag 2022;1:1. https://doi.org/10.1504/IJMRI.2022.10046112.

[35] Yuan Y, Milani G. Closed-form model for curved brittle substrates reinforced with FRP strips. Compos Struct 2023;304:116443. https://doi.org/10.1016/j.compstruct.2022.116443.

[36] D'Ambrisi A, Feo L, Focacci F. Experimental and analytical investigation on bond between Carbon-FRCM materials and masonry. Compos Part B-Eng 2013;46:15–20.

[37] Grande E, Imbimbo M, Sacco E. Investigation on the bond behavior of clay bricks reinforced with SRP and SRG strengthening systems. Mater Struct 2015;48(11):3755–70.

[38] Carozzi FG, Colombi P, Fava G, Poggi C. A cohesive interface crack model for the matrix-textile debonding in FRCM composites. Compos Struct 2016;143:230–41.

[39] D'Antino T, Colombi P, Carloni C, Sneed LH. Estimation of a matrix-fiber interface cohesive material law in FRCM-concrete joints. Compos Struct 2018;193:103–12. https://doi.org/10.1016/j.compstruct.2018.03.005.

[40] Calabrese AS, Colombi P, D'Antino T. Analytical solution of the bond behavior of FRCM composites using a rigid-softening cohesive material law. Compos B Eng 2019;174:1–10. https://doi.org/10.1016/j.compositesb.2019.107051.

[41] Zou X, Sneed LH, D'Antino T. Full range behavior of fiber reinforced cementitious matrix (FRCM)-concrete joints using a trilinear bond-slip relationship. Compos Struct 2020;239:#112024.

[42] Calabrese AS, D'Antino T, Colombi P. Experimental and analytical investigation of PBO FRCM-concrete bond behavior using direct and indirect shear test set-ups. Compos Struct 2021;267. https://doi.org/10.1016/j.compstruct.2021.113672.

[43] Bertolli V, D'Antino T. Modeling the behavior of externally bonded reinforcement using a rigid-trilinear cohesive material law. Int J Solid Struct 2022;248:111641. https://doi.org/10.1016/j.ijsolstr.2022.111641.

[44] Grande E, Imbimbo M, Sacco E. Numerical investigation on the bond behavior of FRCM strengthening systems. Compos B Eng 2018;145:240–51. https://doi.org/10.1016/j.compositesb.2018.03.010.

[45] Grande E, Milani G. Interface modeling approach for the study of the bond behavior of FRCM strengthening systems. Compos B Eng 2018;141:221–33. https://doi.org/10.1016/j.compositesb.2017.12.052.

[46] Milani G, Grande E. Simple bisection procedure in quickly convergent explicit ODE solver to numerically analyze FRCM strengthening systems. Compos B Eng 2020; 199:108322. https://doi.org/10.1016/j.compositesb.2020.108322.
[47] Grande E, Milani G. Procedure for the numerical characterization of the local bond behavior of FRCM. Compos Struct 2021;258:113404. https://doi.org/10.1016/j.compstruct.2020.113404.
[48] Grande E, Milani G, Imbimbo M. Theoretical model for the study of the tensile behavior of FRCM reinforcements. Construct Build Mater 2020;236:#117617.
[49] Grande E, Imbimbo M, Sacco E. Bond behaviour of CFRP laminates glued on clay bricks: experimental and numerical study. Compos B Eng 2011;42(2):330–40.
[50] Ghiassi B, Oliveira DV, Lourenço PB, Marcari G. Numerical study of the role of mortar joints in the bond behavior of FRP-strengthened masonry. Compos B Eng 2013;46:21–30. https://doi.org/10.1016/j.compositesb.2012.10.017.
[51] Razavizadeh A, Ghiassi B, Oliveira DV. Bond behavior of SRG-strengthened masonry units: testing and numerical modeling. Construct Build Mater 2014;64: 387–97. https://doi.org/10.1016/j.conbuildmat.2014.04.070.
[52] Bertolesi E, Milani G, Fagone M, Rotunno T, Grande E. Micro-mechanical FE numerical model for masonry curved pillars reinforced with FRP strips subjected to single lap shear tests. Compos Struct 2018;201:916–31.
[53] Carozzi FG, Milani G, Poggi C. Mechanical properties and numerical modeling of Fabric Reinforced Cementitious Matrix (FRCM) systems for strengthening of masonry structures. Compos Struct 2014;107:711–25.
[54] Bertolesi E, Carozzi FG, Milani G, Poggi C. Numerical modeling of fabric reinforce cementitious matrix composites (FRCM) in tension. Construct Build Mater 2014; 70:531–48.
[55] Grande E, Ghiassi B, Imbimbo M. Chapter 19 - theoretical and FE models for the study of the bond behavior of FRCM systems. In: Ghiassi B, Milani G, editors. Numerical modeling of masonry and historical structures. Woodhead Publishing; 2019. p. 685–712. https://doi.org/10.1016/B978-0-08-102439-3.00019-1.
[56] Scacco J, Milani G, Lourenço PB. A micro-modeling approach for the prediction of TRM bond performance on curved masonry substrates. Compos Struct 2021;256: 113065. https://doi.org/10.1016/j.compstruct.2020.113065.
[57] Yu C, Hoogenboom PCJ, Rots JG. Incremental sequentially linear analysis to control failure for quasi-brittle materials and structures including non-proportional loading. Eng Fract Mech 2018;202:332–49. https://doi.org/10.1016/j.engfracmech.2018.07.036.
[58] Pari M, Swart W, van Gijzen M, Hendriks M, Rots J. Two solution strategies to improve the computational performance of sequentially linear analysis for quasi-brittle structures. Int J Numer Methods Eng 2020;121:2128–46. https://doi.org/10.1002/nme.6302.
[59] Pari M, Hendriks MAN, Rots JG. Non-proportional loading in sequentially linear solution procedures for quasi-brittle fracture: a comparison and perspective on the mechanism of stress redistribution. Eng Fract Mech 2020;230:106960. https://doi.org/10.1016/j.engfracmech.2020.106960.
[60] Pari M, Van de Graaf AV, Hendriks MAN, Rots JG. A multi-surface interface model for sequentially linear methods to analyse masonry structures. Eng Struct 2021; 238:112123. https://doi.org/10.1016/j.engstruct.2021.112123.
[61] Yu C, Hoogenboom P, Rots J. Extension of incremental sequentially linear analysis to geometrical non-linearity with indirect displacement control. Eng Struct 2021; 229:111562. https://doi.org/10.1016/j.engstruct.2020.111562.